

Interaction of two-phase debris flow with obstacles

Parameshwari Kattel^{a,b}, Jeevan Kafle^{a,c}, Jan-Thomas Fischer^d, Martin Mergili^{e,f},
Bhadra Man Tuladhar^a, Shiva P. Pudasaini^{g,*}

^a School of Science, Kathmandu University, Dhulikhel, Kavre, Nepal

^b Department of Mathematics, Tri-Chandra Multiple Campus, Tribhuvan University, Kathmandu, Nepal

^c Central Department of Mathematics, Tribhuvan University, Kathmandu, Nepal

^d Austrian Research Center for Forests-BFW, Department of Natural Hazards, Rennweg 1, 6020 Innsbruck, Austria

^e Institute of Applied Geology, University of Natural Resources and Life Sciences (BOKU), Vienna, Austria

^f Geomorphological Systems and Risk Research (ENGAGE), Department of Geography and Regional Research, University of Vienna, Universitaetsstrasse 7, 1010 Vienna, Austria

^g Department of Geophysics, Steinmann Institute, University of Bonn, Meckenheimer Allee 176, D-53115 Bonn, Germany

ARTICLE INFO

Keywords:

Two-phase debris flows
Flow-obstacle-interactions
High-resolution numerical simulations
Shock waves
Impact vacuum

ABSTRACT

Landslides, debris avalanches and flows are common events in mountainous regions, causing tremendous damages to people and infrastructures. Their dynamics are substantially affected and altered by obstacles such as trees, big boulders and civil structures on their way. Appropriately designed and optimally installed obstacles, including braking mounds, catching or deflecting dams, in the flow path can drastically change the flow dynamics by deflecting, re-directing or stopping the debris mass. Such structures can substantially reduce the kinetic energy of the flow and associated risks. So, a proper understanding of the flow-obstacle-interaction is required to construct adequate defense structures. Here, we simulate a two-phase debris flow as a mixture of solid particles and viscous fluid down an inclined surface with tetrahedral obstacles of different dimensions, numbers and orientations. This is achieved by employing a physically-based general quasi-three dimensional two-phase mass flow model (Pudasaini, 2012) consisting of a set of non-linear and coupled partial differential equations representing mass and momentum conservations for both the solid- and fluid-phases. Simulations on mass flows are performed with a high-resolution and efficient numerical scheme that is capable of capturing rapid and detailed dynamics, including the strongly re-directed flow with multiple stream lines, mass arrest, strong shock waves and debris-vacuum generation and flow pattern formations, as the rapidly cascading mass suddenly encounters the obstacles. The estimated impact pressure is useful for designing the defense structures. The solid and fluid phases show fundamentally different interactions with obstacles, flow spreading and dispersions, and run-out dynamics and deposition. The observations are in line with natural debris flows and experiments. Our understanding of the complex interactions of real two-phase mass flows with multiple obstacles helps us to plan defense structures and constitute advanced and physics-based engineering solutions for the prevention and mitigation of risks caused by different gravitational mass flows.

1. Introduction

Various types of gravitational mass movements such as landslides, debris flows, rock falls and flash floods occur in mountainous areas worldwide. Often due to heavy rainfall, loose mass of sediment are saturated with water and flow downslope in response to gravity, resulting in a debris flow or a related phenomenon (Takahasi, 1991). The rapid motion, and especially the interactions between the solid and water provide a debris flow destructive power and a much longer run out than other gravitational mass flows (Takahasi, 1991; Takahashi,

2007; Iverson, 1997; Pitman and Le, 2005).

Debris flows can claim human lives and destroy civil structures, transportation and communication links. Appropriate risk mitigation strategies are essential to reduce those losses (Pudasaini and Hutter, 2007). A common way to mitigate the debris flow hazard is to let the flowing mass impact rigid structures. To mitigate from debris impacts, structural defense measures are used to obstruct or retain landslide debris, reduce debris mobility or to deflect the direction of flow (Hung et al., 1987; Pudasaini and Hutter, 2007; Johannesson et al., 2009; Cui et al., 2015). The importance of structural defense measures in

* Corresponding author.

E-mail address: pudasaini@geo.uni-bonn.de (S.P. Pudasaini).

gravitational mass flow context is mainly for protecting civil structures or settlements from avalanches and debris flows. Defense measures may include single or multiple units of structures like rigid and flexible barriers, braking mounds, catching or deflecting dams and baffles (Hungre et al., 1984; Teufelsbauer et al., 2009; Naaim et al., 2010; Teufelsbauer et al., 2011). Deflecting dams and structures in terms of wedge obstacles can divert the flow away from the high risk area to a low risk area. Braking or retarding mounds cause increased dissipation of kinetic energy, thereby reducing the speed and run out. Deflecting and dissipating defense structures are generally constructed in the track zone and also in the run out zones to divert, retard or stop a moving debris mass before it leads to damages downstream (Hungre et al., 1987; Pudasaini and Hutter, 2007; Faug et al., 2008). The location, size and the strength of the defense structure depend upon the slope and anticipated volume of the debris flows, their type and velocity, and the nature of the object or the area to be protected (Pudasaini and Hutter, 2007; Johannesson et al., 2009; Faug et al., 2010). Flow-obstacle-interactions are processes causing sudden change in flow-regimes (Faug, 2015). If defense structures are installed more upstream, they can protect more area downstream by deflecting the debris mass wider with reduced or no deposition around it. However, they are sometimes aligned at low gradients to increase deposition around them to reduce the run out length of the debris flow (Faug et al., 2003, 2008; Pudasaini and Hutter, 2007; Gleirscher and Fischer, 2014). If an obstacle is high enough and prevents the flow overtopping, a propagating normal shock and semi-stationary oblique shock may form upstream of the obstacle (Tai et al., 2001; Gray et al., 2003; Hákonardóttir and Hogg, 2005; Johannesson et al., 2009; Faug et al., 2010; Faug, 2015).

Due to the complex evolving behaviour of debris flow, a single rheological model equation is not sufficient to describe it. Various rheological models were proposed in the past, but they were effectively single-phase models (Takahashi, 1991; Iverson, 1997). There have been significant fundamental research activities in the past few decades in the field of debris flows and similar mass flows, e.g., (i) single-phase dry granular avalanches (Savage and Hutter, 1989; Hungre, 1995; Hutter et al., 1996; Gray et al., 1999; Pudasaini and Hutter, 2007), (ii) single-phase debris flows (Bagnold, 1954; Chen, 1988; O'Brien et al., 1993; Takahashi, 2007), (iii) mixture flows (Iverson, 1997; Iverson and Denlinger, 2001; Pudasaini et al., 2005a), (iv) two-fluid debris flow (Pitman and Le, 2005), and (v) a two-layered model (Fernandez-Nieto et al., 2008).

A major advancement in two-phase debris flow modelling and simulation is made by Pudasaini (2012) by proposing a comprehensive theory and simulation technique (Pudasaini, 2014; Pudasaini and Krautblatter, 2014). The model includes interactions between the solid and the fluid constituents. Along with buoyancy, the model also includes three other dominant physical aspects of flow: enhanced non-Newtonian viscous stress induced by gradient of solid volume fraction, virtual mass and generalized drag (Pudasaini, 2012). Because of these features, here we use this model to simulate the interaction of two-phase debris flow with obstacles. The model equations are presented in the Appendix. Some major aspects of the model are briefly mentioned here. The fluid pressure and simple drag between the solid and the fluid phases have been included in some of the previous models (Iverson and Denlinger, 2001; Pitman and Le, 2005; Pudasaini et al., 2005a). However, they do not include the following three dominant physical features that can be observed in real two-phase debris flows in nature. (i) As the two phases generally have different velocities, they may have non-zero relative accelerations, too. In particular, if the solid particles accelerate relative to the fluid, a part of the ambient fluid is also accelerated, thereby inducing a virtual mass force (the change in the kinetic energy of the fluid). This force has been incorporated in debris flow dynamics for the first time by Pudasaini (2012). (ii) Another important physical aspect that has been exclusively included in Pudasaini (2012) model is the non-Newtonian viscous stress due to gradients in the volume fraction of solids. Indeed, the quantity and gradient of the

solid particles can either enhance or downplay the viscous effects in the flow. This influences the flow substantially. (iii) In this model (Pudasaini, 2012), a new generalized drag coefficient has been developed that covers both linear and quadratic drags. As the material composition evolves in time and space in a real two-phase debris flow, leading to solid-dominated (more solid material than fluid) or fluid-dominated local regions in the same debris body, the drag forces in the debris flows can only be properly modelled and described by applying a generalized drag force (Pudasaini, 2012).

Being based on the general two-phase mass flow model of Pudasaini (2012), many realistic simulations of two-phase debris flows in down-slope direction (Pudasaini, 2012) and both downslope and cross slope directions (Kattel et al., 2016), and submarine debris flows (Pudasaini, 2014; Kafle et al., 2016) have been carried out. While all these simulations were performed on idealized generic topographies, Mergili et al. (2017) presented the GIS-based application r.avaflow, enabling the application of the model approaches to real flow events in mountain topographies.

Obstacle interactions are mostly discussed for granular flows (Tai et al., 2001; Wawra, 2010; Cui and Gray, 2013; Viroulet et al., 2017), or for a debris bulk without considering two separate phases (Xie et al., 2014; Cui et al., 2015; Piton and Recking, 2016). Hákonardóttir et al. (2003a, 2003b, 2003c), Hákonardóttir (2004), Johannesson et al. (2009) and Faug (2015) experimentally showed that a part of flowing granular mass with high speed detaches from the bed and travel as airborne jet while overtopping an obstacle. In natural debris flows, solid and fluid phases evolve differently and show different dynamic behaviour (Pudasaini, 2012; Mergili et al., 2017, 2018). The solid and fluid phases may interact in different ways with obstacles. This results in completely different solid and fluid dynamics around and downstream of obstacles. Nevertheless, almost all the studies so far concern single-phase flows and obstacle interactions. Therefore, our present study of two-phase flow interaction with obstacles is novel and expected to be important for the proper understanding of the separate but simultaneous interactions with the obstacles and dynamical behavior of the solid and fluid constituents in the debris-mixture.

Figure 1A is a photograph of braking mounds and the catching dam in eastern Iceland as an example of integrated obstacles. The system has thirteen 10 m high breaking mounds with steep upper faces in two staggered rows. The catching dam is 17 m high and 400 m long (Johannesson et al., 2009). Such obstacles are commonly used mitigation measures for protection against avalanches. They reduce the speed and the run out of the flow and stop or retard some portion of the mass. Figure 1B is a small scale laboratory model developed by Naaim et al. (2010) for an experiment to study and optimize the mounds in terms of energy dissipation and flow spreading of the granular avalanche at the beginning of the run out zone. They performed the experiments with different number and spacing of mounds, and best result for run out shortening and flow spreading was observed with two large mounds with a large open section between them. Debris flows are, in some extent, comparable with snow avalanches and granular flows as they can sustain shear stresses with slow deformation and can flow rapidly (Gleirscher and Fischer, 2014). Such installation as in Fig. 1 can also be utilized to study debris flow-obstacle-interactions.

Here, we conduct a number of computational experiments on the detailed dynamical interaction of the flowing debris with a stationary tetrahedral obstacle mounted on a generic slope surface running out into a horizontal plane. We describe the run out scenarios for solid and fluid phases separately and for a debris bulk as a whole. For this, we consider a tetrahedral obstacle with different orientations, numbers, sizes and spacing to demonstrate different types of flow-obstacle-interactions. In a numerical experiment, we also compute the dynamic impact pressure not only from the density and the velocity of the mixture, but also a barycentric impact pressure from the solid- and fluid- phases pressures. Although dynamical aspects including impact pressure, momentum loss and energy dissipation are very important

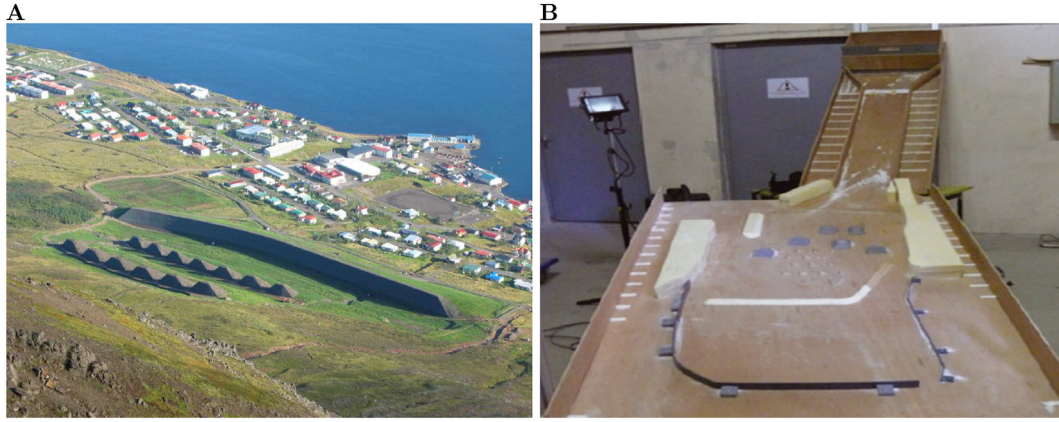


Fig. 1. A: Braking mounds and a high steep catching dam in eastern Iceland (Johannesson et al., 2009). B: Photograph of the small-scale physical model of the run out zone with integrated obstacles; the granular material is stored at the top before release (Naaim et al., 2010).

quantitative aspects of study in obstacle interactions, here, we especially focus on the geometrical aspects of interactions, mainly the evolution of solid and fluid flow depths in the vicinity of the obstacles, the deflections and the change in run out distances and the inundation areas. The key objective of the study is to characterize the effects of the various types of configuration of the obstacles in order to add on information on risk mitigation.

In Section 2, we present the simulation set-up and the choice of parameters. We discuss the simulation results in Section 3, with a reference simulation without obstacle. As a single obstacle in the flow path, we consider a forward-facing and a rearward-facing tetrahedra and present the different flow-obstacle-interactions. The interaction and the subsequent flow dynamics due to a system of tetrahedral obstacles are also investigated. In Section 4, we compare our results with some experiments for obstacle interaction with granular flows found in existing literatures with some similarities and differences with our numerical experiments for the interaction of two-phase debris flow with obstacles. In Section 5, we present summary of our present study.

2. Simulation set-up of flow-structure-interaction

2.1. Topography

We consider a topography as a slope surface from $x = x_0$ to $x = x_r$, inclined at an angle ζ_0 , that follows a horizontal run out zone from $x = x_r$ to $x = x_f$ as shown in Fig. 2A. Simulations are carried out by releasing the debris, which then flows down to the run out zone.

2.2. The obstacles

We consider triangular pyramids (or, tetrahedra) of different numbers, sizes and orientations as obstacles. Tetrahedra are efficient deflecting and dissipating structures. In general, debris flow front impacts the bottom and middle part of a high structure on its way, subjected to higher shearing or bending of the structure at the impact location (Zeng et al., 2014; Cui et al., 2015). So, dissipating or deflecting structures must be strong at the base. Moreover, as we will see later, the differently oriented tetrahedral obstacles in the flow path can deflect the desired amount of solid and fluid component in the mixture in the desired directions and amount or stop the debris mass. Because of this, tetrahedral obstacles can be appropriate deflecting and dissipating structures.

A particular pyramid or tetrahedron as shown in Fig. 2B has a triangular base with vertices $A(x_1, y_1, 0)$, $B(x_2, y_2, 0)$ and $C(x_3, y_3, 0)$. If the apex is at $D_{\text{apex}}(x_4, y_4, d)$, then its projection on the xy -plane is $D(x_4, y_4, 0)$, where d is the height of the tetrahedron measured in the direction normal to the slope.

To compute the gradients of the three faces, the normal height b of the topography above the flow-plane is given by the following.

(I) For the flank ABD_{apex} :

$$b(x, y) = d \frac{(x - x_1)(y_1 - y_2) - (y - y_1)(x_1 - x_2)}{(x_2 - x_1)(y_4 - y_1) - (y_2 - y_1)(x_4 - x_1)},$$

where

$$y < y_1 + \frac{y_4 - y_1}{x_4 - x_1}(x - x_1), \quad \text{for } x \in [x_1, x_4],$$

$$y < y_2 + \frac{y_4 - y_2}{x_4 - x_2}(x - x_2), \quad \text{for } x \in [x_4, x_2],$$

$$y > y_1 + \frac{y_2 - y_1}{x_2 - x_1}(x - x_1), \quad \text{for } x \in [x_1, x_2].$$

(II) For the flank ACD_{apex} :

$$b(x, y) = d \frac{(x - x_1)(y_1 - y_3) - (y - y_1)(x_1 - x_3)}{(x_3 - x_1)(y_4 - y_1) - (y_3 - y_1)(x_4 - x_1)},$$

where

$$y > y_1 + \frac{y_4 - y_1}{x_4 - x_1}(x - x_1), \quad \text{for } x \in [x_1, x_4],$$

$$y > y_3 + \frac{y_4 - y_3}{x_4 - x_3}(x - x_3), \quad \text{for } x \in [x_4, x_3],$$

$$y < y_1 + \frac{y_3 - y_1}{x_3 - x_1}(x - x_1), \quad \text{for } x \in [x_1, x_3].$$

(III) For the flank BCD_{apex} :

$$b(x, y) = d \frac{(x - x_2)(y_2 - y_3) - (y - y_2)(x_2 - x_3)}{(x_3 - x_2)(y_4 - y_2) - (y_3 - y_2)(x_4 - x_2)},$$

where

$$y > y_2 + \frac{y_4 - y_2}{x_4 - x_2}(x - x_2), \quad \text{for } x \in [x_4, x_2],$$

$$y < y_3 + \frac{y_4 - y_3}{x_4 - x_3}(x - x_3), \quad \text{for } x \in [x_4, x_3],$$

$$x < x_2 + \frac{x_3 - x_2}{y_3 - y_2}(y - y_2), \quad \text{for } y \in [y_2, y_3].$$

In (I)–(III), x and y represent the coordinates along the downslope and the cross slope directions, respectively describing the tetrahedra. The inequality signs may change/reverse according as the orientations of the tetrahedra.

The slope fitted coordinates could better incorporate the geometrical effects of the channel into the flow dynamics. For example, this enhances the normal load, and thus the Coulomb friction force. In the past, such effects have been exclusively incorporated into the model equations by applying the curvilinear coordinates with smooth changes of the slope that included curvature along the longitudinal direction (Savage and Hutter, 1991; Gray et al., 1999) for dry granular flows; and curvature and twist along the longitudinal and transversal directions for

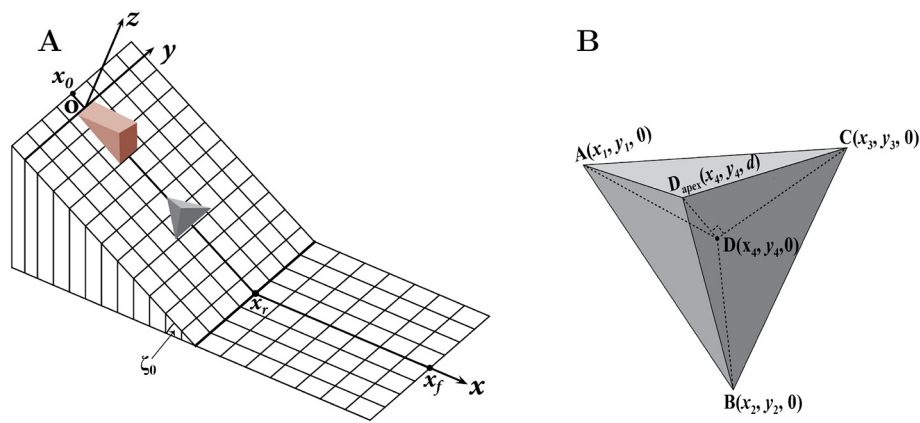


Fig. 2. A: Initial set up showing the flow domain, that starts with a slope $[x_0, x_r]$ inclined at an angle of ζ_0 with the horizontal, followed by a horizontal run out $[x_r, x_f]$; O is the origin. The initial debris in brown encounters a tetrahedral obstacle in gray when it is triggered and flows downstream. B: A general triangular pyramid (tetrahedron) as an obstacle. Different positions of the vertices A, B, C and the apex D_{apex} can vary the size and orientation of the tetrahedron. The projection of the apex, D_{apex} on the base is D .

granular and debris flows down general channels (Pudasaini and Hutter, 2007; Pudasaini et al., 2005a, 2005b). Particularly, Pudasaini et al. (2005a) exclusively studied the effects of the channel into the flow dynamics through the two-directional curvature and twist. Simulation of the debris flow-obstacle-interaction is a new direction in mass flow research. So, here, we begin with the most simple and idealized geometrical setting by considering the flow down an inclined slope that is connected to the horizontal plane. Due to this particular setting, the curvature virtually does not appear into the dynamics. This also applies to the obstacles since the tetrahedral pyramids used here change the slope abruptly from the channel. So, from a technical point of view, we have disregarded the centrifugal forces for such obstacles. Furthermore, the path fitted coordinates, although probably are the best from the theoretical point of view, it is technically less appropriate to be applied to define the obstacles with abrupt changes in the slopes from the reference surface, such as the vertical walls and (substantially sloped) tetrahedron as used here. Nevertheless, this has been achieved here by utilizing the gradients of the obstacles in the coordinate directions as included in the source terms (7)–(10) of the model by the terms $\partial b/\partial x$, and $\partial b/\partial y$ (see, Appendix). However, following the locally slope fitted coordinates as in Fischer et al. (2012), Pudasaini (2012) and Mergili et al. (2018), in further contributions, we may include the curvature of the slope by considering the smooth transition of the slope both in the longitudinal and transversal directions. Here, the flow obstruction due to obstacles is implemented in the model by the local height changes in the basal topography (Wawra, 2010; Pudasaini, 2012). As the flow impacts and interacts with the obstacle, the gradient of the tetrahedron ($\partial b/\partial x$, $\partial b/\partial y$) acts against the flow, thereby inducing a resisting/re-directing force.

2.3. Simulation set-ups

For all the simulations, we consider the same initial set ups of channel geometry and debris mass, and physical and material parameters but with different obstacle configuration. The spatial domain for simulation ranges from $x_0 = -25$ m to $x_f = 450$ m in the downstream direction and from $y = -200$ m to $y = 200$ m in the cross wise direction. The plane is inclined at an angle of $\zeta_0 = 45^\circ$ from $x_0 = -25$ m to $x_r = 160$ m, that follows a horizontal run out zone from $x_r = 160$ m to $x_f = 450$ m (Fig. 2A). The initial debris mass is defined by a triangular wedge $0 \text{ m} \leq x \leq 50 \text{ m}$, $-15 \text{ m} \leq y \leq 15 \text{ m}$ that contains a homogeneous mixture of solid (75%) and fluid (25%).

2.4. Parameter choice and numerical method

The model is described in Appendix that contains several parameters. The common parameters chosen for all the simulation results presented here are: $\phi = 35^\circ$, $\delta = 15^\circ$, $\mathcal{U}_T = 1.0$, $Re_p = 1$, $\mathcal{P} = 0.45$, $J = 1$, $\mathcal{C} = 0.4$, $N_R = 30,000$, $N_{R_\omega} = 1,000$, $\chi = 3$ and $\xi = 5$. The solid

and fluid densities are taken as $\rho_s = 2,800 \text{ kg m}^{-3}$ and $\rho_f = 1,100 \text{ kg m}^{-3}$. These choices of parameters are made on the basis of the physics of two-phase subaerial and submarine mass flows as discussed in Iverson and Denlinger (2001), Pudasaini (2012), Pudasaini and Krautblatter (2014), Kattel et al. (2016) and Mergili et al. (2017). In different simulations, the obstacles differ at least in one of the sizes, orientations and numbers.

Gravitational mass flows generally are in rapid motion, can have several encounters with obstacles, large deformations and abrupt changes in flow dynamical variables. In order to capture such complicated phenomena, we employ high-resolution Total Variation Diminishing (TVD) Non-Oscillatory Central (NOC) schemes (Tai et al., 2002) to numerically integrate the model Eqs. (1)–(6), which are efficient even when shocks are produced (Nessyahu and Tadmor, 1990; Jiang and Tadmor, 1998; Lie and Noelle, 2003; Pudasaini and Hutter, 2007; Mergili et al., 2017, 2018).

3. Simulation results and discussions

Usually a debris flow model allows us to compute the primary flow variables, such as flow velocity and depth for solid and fluid. So, in terms of two phase model, we can also determine evolving bulk density. These quantities are used to specify impact pressures and flow energies. So, a debris flow model can be utilized to compute the impact force or the maximum impact pressure and the pressure distribution over the obstacles and the change of dynamics of the flow due to obstacles (Cui et al., 2015; Sovilla et al., 2016). The interaction between the flow and the obstacles largely depends on the obstacle geometry and the type and volume of the flow. Calculation of the impact pressure requires the debris height, the bulk density and the velocity of the flow during the impact. These quantities are obtained from the process based model which describes the flow behavior along the slope. The process based models also characterize the interaction between the flow, the channel and the obstacle surfaces (Gray et al., 2003; Cui et al., 2015). Most of the available process based models treat debris as a single bulk and they do not describe the explicit evolution of the solid and fluid phases and their interactions with the obstacles as observed in natural debris flows.

Here, we use the general two-phase mass flow model (Pudasaini, 2012) to present simulations of the explicit and simultaneous evolutions of the solid and fluid phases and the interaction of total debris mass with different configurations of tetrahedral obstacles. In what follows, we describe the interaction of the two phase debris flows with different configurations of tetrahedral obstacles. We begin with undisturbed flow without obstacle in the path as a reference.

3.1. Undisturbed flow

At $t = 0$ s, the debris mass begins to deform and move under the action of gravity and pressure gradient, thereby generating a rapidly

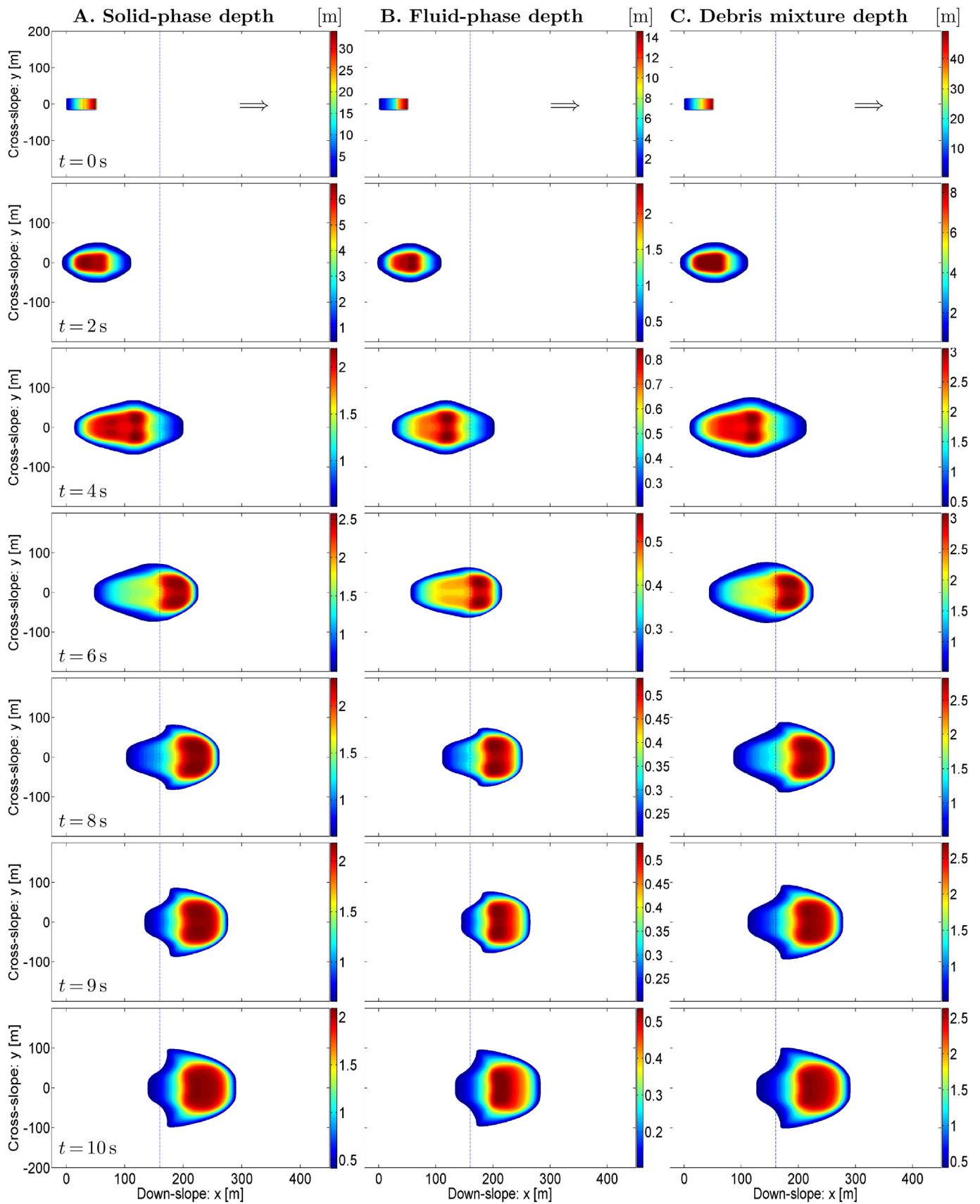


Fig. 3. No Obstacle: Evolution of A. Solid phase, B. Fluid phase, C. Total debris mixture at $t = 0, 2, 4, 6, 8, 9,$ and 10 s as an initial homogeneous debris mixture of solid and fluid is triggered. In the absence of obstacle in the flow path, the undisturbed solid 75%, fluid 25% and total debris mass are advecting downslope substantially and also dispersing in cross-stream direction as time progresses. The solid and fluid phases show different flow dynamics and run out morphology. The arrows in the top panels indicate the flow direction. The blue dashed line in each panel indicates the transition from the inclined plane to the horizontal run out.

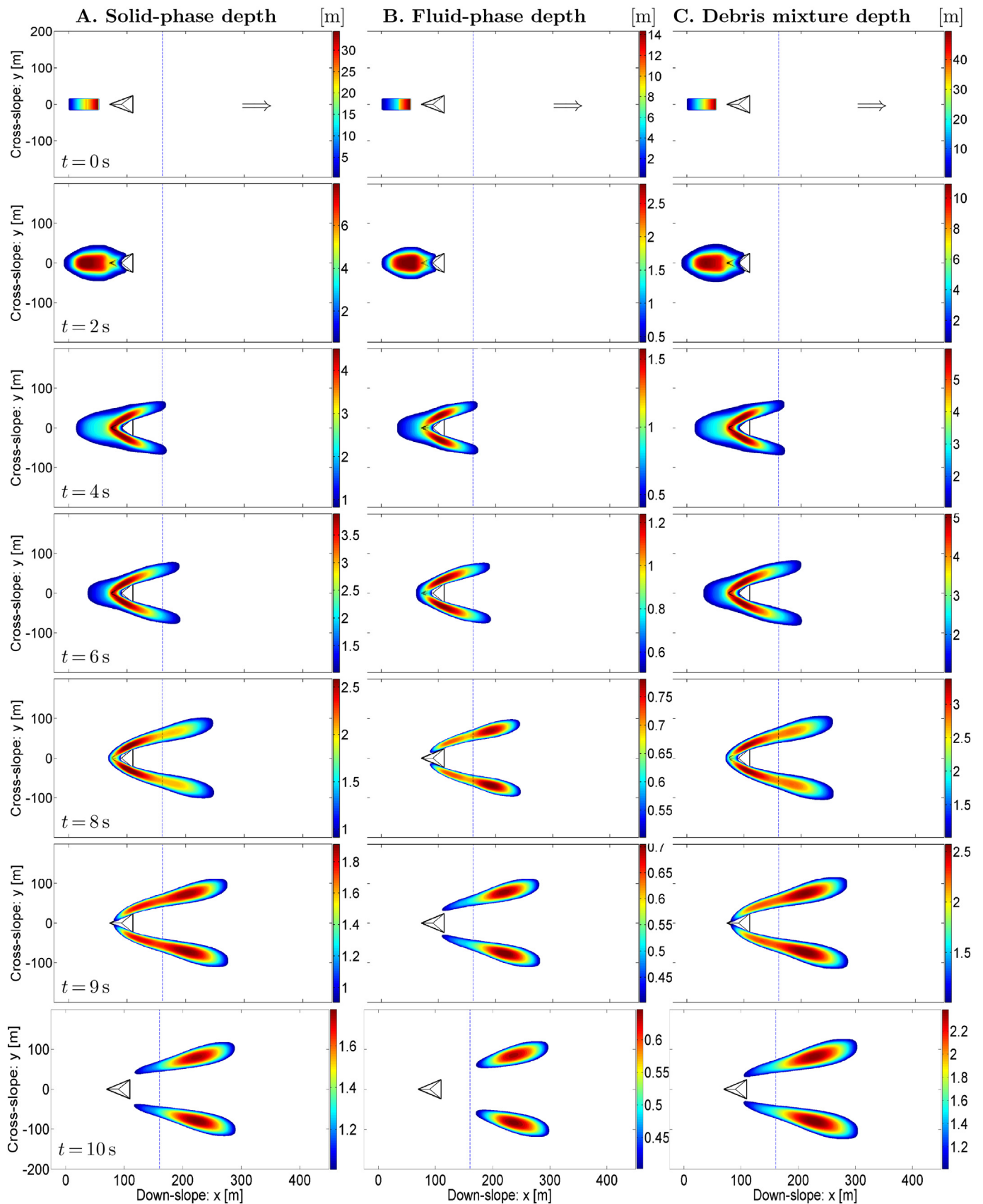


Fig. 4. Forward-facing tetrahedron: Evolution and flow-obstacle-interaction of A. Solid phase, B. Fluid phase, C. Total debris mixture at $t = 0, 2, 4, 6, 8, 9$ and 10 s as a debris flow is triggered and hits a forward-facing tetrahedral obstacle. The arrows in the top panels indicate the flow direction. The blue dashed lines indicate the transition from the inclined plane to horizontal run out. The debris flow is deflected wide apart into two streamed lobes creating impact vacuum behind the obstacle, thereby mitigating the wider area around the central part. The front nose of the tetrahedron interacts and momentarily holds more solid than fluid. This results in completely different interacting behaviour of solid and fluid phases.

moving debris flow. First, we analyze the flow of the solid phase as given in Fig. 3A. As soon as the debris mass starts moving at $t = 0$ s, the solid advects and disperses (spreads) in the downstream and also in the cross stream directions. We also observe that, due to pressure gradient, a little bit of solid mass also moves up-hill ($t = 2$ s). The downslope advection and the cross slope dispersion of solid mass is more pronounced as time progresses. At $t = 4$ s, the solid part of the debris body has widely spread from the middle to the rear part of the debris body. From $t = 4$ s to $t = 6$ s, the major part of the solid mass crosses the slope and the transition zone and advects toward the run-out zone forming a strong surging head along with a longer tail at the rear part of the debris body. In fact, at $t = 6$ s, the debris flow transports the solid phase from the debris body to the frontal debris flow head. For $t > 4$ s, in the absence of the slope, the flow decelerates and due to the reduced gravity, the flow comes to the flow pattern defining the deposition by friction. As the solid main body behind the head moves faster than the solid head itself, more solid mass gets accumulated at solid head at $t = 8$ s. Due to the decelerating flow and friction, the rate of advection of the solid mass in the downslope distance starts to strongly decrease from $t = 8$ s onward. Almost all solid mass flows into run out zone and ultimately comes to a halt.

Next, we analyze the dynamics of the fluid flow (Fig. 3B). When the debris mass collapses, the fluid also advects downstream and spreads. At $t = 2$ s, the relative maximum of the fluid phase lies in the middle part of the debris body. From $t = 8$ s onward, the fluid gets decelerated in the run-out zone. The spreading of fluid mass in cross stream direction is more pronounced than its advection in the downstream direction. The increased solid volume fraction at the frontal debris enhances the non-Newtonian viscous stress, thereby causing more hindrance of the fluid flow. So, the fluid front and the fluid maximum travel less far downslope distance than the solid. The run out morphology of the fluid mass is substantially changing from $t = 6$ s to $t = 10$ s. As the solid phase virtually does not move for $t > 10$ s, we stop the simulation. Nevertheless, for full stoppage of the solid and the fluid run-off, sophisticated depositional models are required (Pudasaini and Fischer, 2016a; Mergili et al., 2017, 2018). However, it is not within the scope of this paper to deal with these aspects.

Figure 3C shows the evolution of the total debris depth, which is dynamically more important. Although the time evolution and dynamics of the total debris bulk (C) is the sum of the solid-phase (A) and the fluid-phase (B), the dynamics is more similar to that of solid due to the composition of the initial debris mixture (more solid than fluid). As soon as the debris flow is released, the maximum of total debris bulk lies in the middle to rear part of the debris body. As in unconfined free-surface mass flows in the slope, the debris mass develops into more ellipsoidal form. At $t = 6$ s, the front gets wider but the rear part gets relatively narrower. The front part is relatively solid-rich and mechanically stronger than the relatively fluid-rich longer tail of the rear part. At $t = 6$ s, the debris flow gets matured, as there is less water content at the head (Lyu et al., 2017). From $t = 8$ s onwards, the low flux and the slope reducing to the zero angle for the run-out zone lead to the paraboloid-type deposition of the total debris bulk. From $t = 8$ s to $t = 10$ s, the frontal debris head moves a very small downslope distance due to the lower momentum, lateral pressure, friction and support from the frontal head.

3.2. Flow past a single obstacle

A. Forward-facing tetrahedral obstacle:

For this simulation (Fig. 4), the stationary obstacle is defined by a tetrahedron having a triangular base with A(70, 0, 0) m as the foremost point and the remaining two vertices at B(110, -24, 0) m and C(110, 24, 0) m. The apex of the tetrahedron is at D_{apex} (90, 0, 30) m. Figure 4 describes the time evolution of the solid depths, fluid depths and (total) debris flow depths along with the obstacle interactions separately.

First, we analyze the flow of the solid phase and its impact on the obstacle as given in Fig. 4A. At $t = 2$ s (A), the solid phase of the debris body has already hit the front and the lateral sides of the tetrahedron, thereby showing lateral deflection (diversion). The deflection continues as the time progresses. For $t > 2$ s, the maximum of the flow begins to develop at the front and around the lateral sides of the obstacle, creating an oblique shock. Behind the obstacle, there is no solid grain, creating granular vacuum. The colour bars alongside in all subplots show that the maximum solid height decreases continuously. From $t = 4$ s to $t = 6$ s, the solid mass is still flowing and impacting the lateral faces of the obstacle and the deflection is more pronounced. The relative maxima lie in the vicinity of the lateral flanks of the obstacle till $t = 8$ s. At $t = 8$ s, the maximum portion of the solid part of the debris body is divided into two elongated lobes that move more downslope. Solid deposition process is seen for $t \geq 8$ s in the run out lobes from the flow front. This results in the continuous migration of the maximum position from the flanks of the obstacle to the run out area with increased grain free area. At $t = 9$ s, the solid mass has two dense surging heads and elongated tails. At $t = 10$ s, the two lobes are already separated with two surging heads with long tails. Although the centres of the relative maxima are at 225 m, the front part of the solid is nearly at 290 m with an average velocity of nearly 20 m s^{-1} .

Next, we analyze the fluid flow dynamics and its interaction with the obstacle (Fig. 4B). At $t = 2$ s, the fluid part also hits the obstacle showing a bit of deflection. The deflection is pronounced as time progresses, since more and more fluid impinges the obstacle. At $t = 4$ s, two relative maxima occur as two deflected streams that travel further cross slope and downslope till $t = 6$ s and decelerate as they begin to reach the run out zone. These two streams are separated at $t = 8$ s, earlier than solid. At $t = 9$ s, the fluid maxima lie on the frontal part of the streams in the run out zone. At $t = 10$ s, the two major portions of the fluid are centered at $x = 250$ m. For $t = 4$ s to $t = 10$ s, the different flow and interacting dynamics of solid and fluid can be seen. The flow obstacle interaction, subsequent dynamics, development of oblique shocks forming lateral lobes, their evolution, propagation and deposition processes are substantially different between the phases. The fluid part travels relatively faster than the solid part as the obstacle retards the solid part more than the fluid part.

Evolution of the total debris mass and its impact on the obstacle have been shown in Fig. 4C as the sum of the solid and fluid mass as given in Fig. 4(A and B). The dynamics of the total debris bulk and its interaction with the tetrahedron is observed somehow as the average of the solid and fluid flow dynamics and interactions. As soon as the debris mass collapses, the total debris bulk disperses in all directions, but substantially in the downstream direction. At $t = 2$ s, the debris has already got impinged at the front nose and the lateral faces of the tetrahedron. As more debris mass flows downstream, the accumulation of the debris in the vicinity of the obstacle increases drastically. It is observed till $t = 6$ s. Due to gravity, the pressure and the momentum of the flowing debris, the slopes of the forward-facing tetrahedral obstacle can not hold the debris mass further. The advection of the debris occurs as two deflected debris streams, thereby creating an impact vacuum (no debris region) (Tai et al., 2001; Gray et al., 2003; Pudasaini, 2014) or a debris vacuum in between. At 9 s, the two deflected debris streams form two surging lobes with longer tails upstream. By $t = 10$ s, the debris flow has completely diverted into two deflected debris streams from the main flow path.

There are several important dynamical aspects between the undisturbed flows and flows interacting with obstacles. First, the flow geometry evolutions are completely different as seen in Fig. 4 as compared to Fig. 3, which is intuitively clear. Something that is counter intuitive is the travel distance. Until $t = 6$ s, the flow front in Fig. 3 moves farther downslope as compared to the flow front in Fig. 4. This can be understood because as the front impacting in Fig. 4 looses some momentum. However, the two frontal surging lobes in Fig. 4 move substantially faster and farther downstream mainly in the run out area.

The fact is that already from $t = 2$ s, and more clearly and evidently from $t = 4$ s, the impact induced shock formation and rapid mass accumulation on both flanks of the tetrahedron resulted in more guided and channelized flows that later developed into very thick lobes much thicker than the undisturbed flow. As the flow is much less dispersive in Fig. 4, the associated hydraulic pressure gradient turned out to be very efficient to increase the mass mobility in the presence of obstacles. Although plausible, such a unique observation is revealed here for the first time for two-phase debris flows.

It is interesting to note that the flow could not over-run the obstacle. In comparison to Fig. 3 (without obstacle), two deflected surging debris streams travel substantially farther downslope. The presence of the forward-facing tetrahedra high in the slope can change the path of the debris flow, shifting the inundation area from around the centre line to the lateral sides of the flow planes in the run out zone. In Fig. 3, the inundation area was from -100 to 100 m in the cross slope direction. Out of it, the region from -50 to 50 m or larger can be mitigated due to the obstacle of this orientation, size and location. As simulated here, a forward-facing tetrahedron, in general, does not permanently capture debris mass. So, this type of obstacle is more suitable in the debris flow prone steep mountain flanks, where the periodic cleaning is very difficult, or almost impossible (Gray et al., 2003; Johannesson et al., 2009).

Next, we compute the approximate impact pressure that the obstacle has to withstand during the flow. Maximum flow depth and maximum flow velocity do not necessarily occur at the same time at a given location. Worst scenario will occur if they coincide (Charvet et al., 2015). We observe that the maximum debris mass interacts the lateral faces of the obstacle at the time slice $t = 4$ s. The bulk density can be computed as $\rho_m = \alpha_s \rho_s + \alpha_f \rho_f = (h_s \times \rho_s + h_f \times \rho_f)/h = (4.4 \times 2800 + 1.6 \times 1100)/6.0 = 2346.7 \text{ kg m}^{-3}$. The acute angle between the flow surface and any one of the two lateral faces of the tetrahedron is $\theta = 29.12^\circ$ approximately. The maximum mixture velocity at $t = 4$ s is $v_m = (\alpha_s v_s + \alpha_f v_f)/\rho_m = (0.7333 \times 2800 \times 20.2 + 0.2667 \times 1100 \times 19.6)/2346.7 = 20.12 \text{ m s}^{-1}$. Then with $h = h_s + h_f = 4.4 + 1.6 = 6$ m, the impact pressure by using (14) is computed as $p_D = (1/2)\rho_m v_m^2 \sin^2 \theta = 112.53 \text{ kPa}$ approximately. The expression for the impact pressure is described in Appendix. This estimated impact pressure is useful to choose the structure shape, dimensions and the appropriate construction material while designing the obstacle. However, note that the impact pressure can also be obtained alternatively as the barycentric pressure (p_{sf}) computed from the solid- and fluid-phase pressures, p_s and p_f . Here, $p_s = (1/2)\rho_s v_s^2 \sin^2 \theta = 135.28 \text{ kPa}$ and $p_f = (1/2)\rho_f v_f^2 \sin^2 \theta = 50.04 \text{ kPa}$. As usual the impact pressure of the solid-phase has dominated that of the fluid-phase. Then, $p_{sf} = (p_s \alpha_s \rho_s + p_f \alpha_f \rho_f)/(\alpha_s \rho_s + \alpha_f \rho_f) = (135.28 \times 0.7333 \times 2800 + 50.04 \times 0.2667 \times 1100)/(0.7333 \times 2800 + 0.2667 \times 1100) = 124.62 \text{ kPa}$.

The two-phase debris flow simulation made it possible to estimate impact pressure in two different ways. However, the above calculation reveals that p_D deviates (underestimates) p_{sf} by about 10.7% which is substantial in application, or for the design of obstacles. From a dynamical point of view p_{sf} is more appropriate, and thus provides more accurate description of impact pressure than p_D . This is so, because unlike p_D , p_{sf} first independently determines the solid and fluid phase pressures, p_s and p_f , which directly use the actual phase-velocities for the solid (u_s) and fluid (u_f). Only then the mixture pressure p_{sf} is determined. However, in p_D the bulk pressure is obtained by utilizing the mixture velocity u_m and that p_D does not explicitly involve the actual phase pressures. Furthermore, u_m is only an average or mean (center of mass) velocity that already loses some information about the actual velocities (u_s , u_f). So, as p_D does not directly involve the phase pressures of solid and fluid, this is dynamically a less accurate description of the impact pressure. From the above calculation it is clear that when the phase-velocities, -volume fractions, and -densities deviate substantially from one phase to another, consequently, p_D also deviates substantially from the more legitimate and realistic description of the impact pressure, p_{sf} . Such an implicit calculation of the mixture pressure from the

knowledge of solid- and fluid-pressures is novel and, from the dynamical perspective, suggests for the use of p_{sf} rather than p_D . Nevertheless, this must be scrutinized and validated with observation or data, which is not a focus here.

B. Rearward-facing tetrahedral obstacle:

Next, we change the orientation of the tetrahedral obstacle. The tetrahedron considered in Fig. 4 is given a half turn about the centre so that the blunt face of the tetrahedron is facing upslope and the sharp face is facing downslope. Now, the front face of the tetrahedron in Fig. 5 is mostly responsible to act against the impact of the debris flow. The vertices of the triangular base are at $(110, 0, 0)$ m, $(70, 24, 0)$ m and $(70, -24, 0)$ m. The apex of the tetrahedron is again at $(90, 0, 30)$ m.

During the initial phase of the flow, the solid part of the debris material flows around the obstacle and develops into an almost steady mass arrest ($t = 4$ s to $t = 6$ s). The topographic gradient of the front face is sufficient enough to substantially dissipate the energy by reducing the momentum of the impinging solid material and hold a substantial portion of it. As time progresses, the deposition (accumulation) increases at the front face of the obstacle (Fig. 5A, $t = 4$ s), thereby creating a dead zone (no flow region) (Gray et al., 2003; Cui and Gray, 2013). After the dead zone was established (after $t = 6$ s), the normal shock which was propagating upslope gets saturated and substantial amount of solid grains gets deflected away from the edges of the tetrahedron into two streams ($t = 8$ s). This results in the decrease of the deposition of the solid in the front of the obstacle (see, Fig. 5A, $t = 6$ s onwards). At the back and the lee side of the obstacle, an impact vacuum is formed. A substantial amount of deposition at the front of the obstacle can still be seen at $t = 10$ s. However, the solid phase is still flowing. No solid mass could be kept as deposition in case of the forward-facing tetrahedron in Fig. 4.

The fluid-phase dynamics (B) and the interaction are loosely similar geometrically to the solid till $t = 6$ s, as a considerable amount of the fluid in the mixture is also stopped by the obstacle. The solid matrix adjacent to the front face of the obstacle hinders the advection and the dispersion of the fluid for a while. However, we can see a larger flow of fluid in the cross stream and the downstream direction at $t = 9$ s. The main deposition lobes are slowly being disconnected from the obstacle. By $t = 9$ s, a substantial amount of fluid has already escaped away from the lateral sides of the obstacle, thereby forming two relatively weak maxima centred nearly at $x = 220$ m. At $t = 10$ s, a completely different obstacle interaction from the solid is seen. The two fluid streams get detached from the obstacle whereas the solid part was still flowing at this time. A small amount of fluid is seen in front of the obstacle at $t = 10$ s that remains there as a part of the mixture. This difference is due to the different material properties and proportion of solid and fluid. Differences mainly emerge from the amount of initial material volume (more solid than fluid), friction for solid and viscosity for fluid. Interestingly, after $t > 6$ s, the fluid moves faster than the solid. This indicates that there was a larger momentum loss for solid at impact than fluid because the solid material is frictional and consumes more energy in frictional dissipation. Although the fluid in the initial material composition is much less than the solid, the downward propagation (after impact) and deposition lobes are quicker and stronger for fluid than solid as seen for $t > 6$ s.

The overall dynamics and obstacle-impact are presented by the evolving and interacting total debris flow depth which is the sum of the solid- and the fluid-phase depths. The obstacle interaction of the total debris body is a bit similar to the solid phase as the amount of solid mass was much greater than the fluid mass in the initial debris. Similar to the solid and fluid phases, there is the formation of dead zone and the debris vacuum (debris material free zone) at the back and the lee side of the obstacle. Here, the debris vacuum on the lee side of the tetrahedron is wider than in the forward-facing tetrahedron (Fig. 4). As the flowing debris mass impacts with the surface with different geometry (blunt and

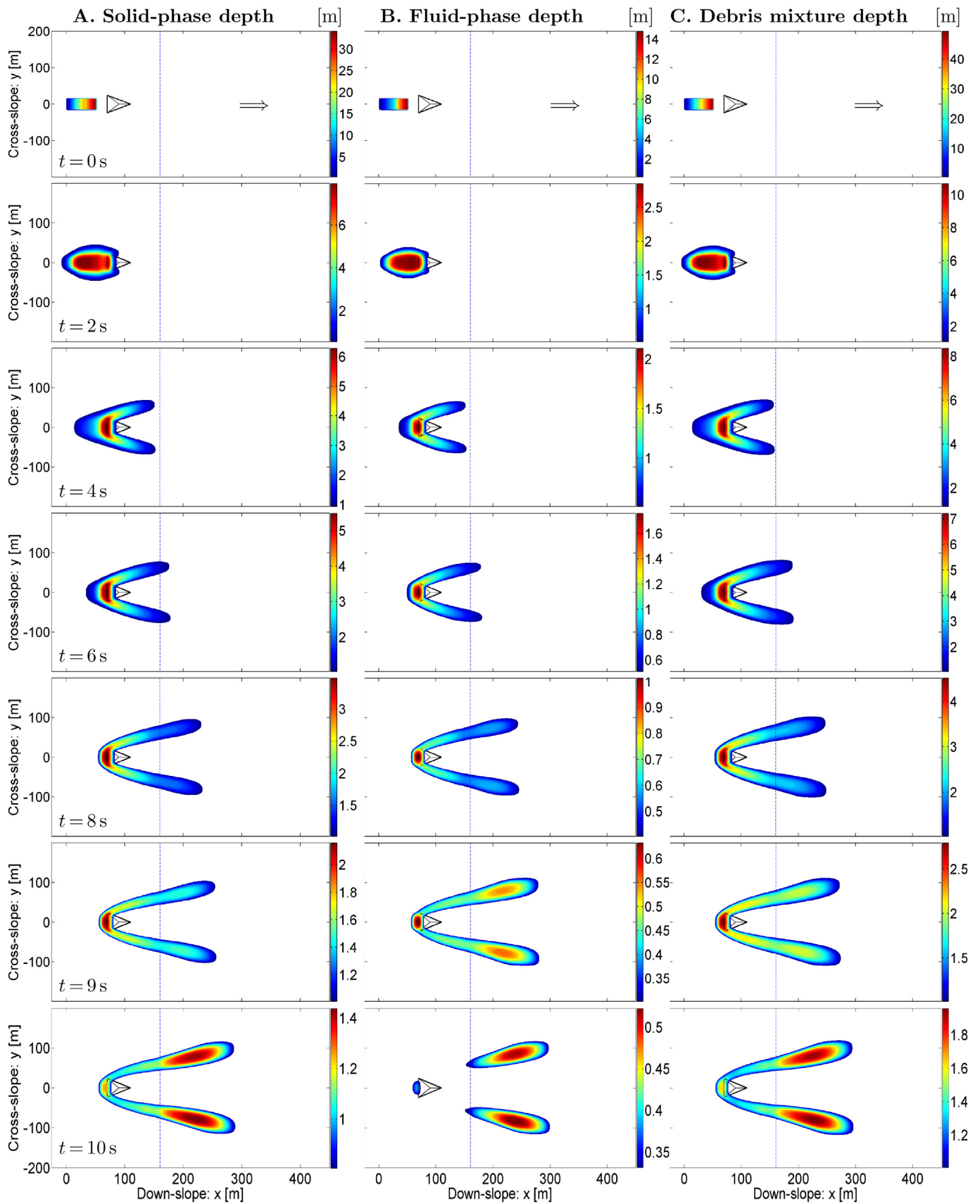


Fig. 5. Rearward-facing tetrahedron: Evolution and flow-obstacle-interaction of A. Solid phase, B. Fluid phase, C. Total debris mixture at $t = 0, 2, 4, 6, 8, 9$ and 10 s as a debris flow is triggered and hits a rearward-facing tetrahedral obstacle. The arrows in the top panels indicate the flow direction. The blue dashed lines indicate the transition from the inclined plane to horizontal run out. Debris vacuum is formed at the back and lee side of the obstacle. A considerable amount of solid mass (also a bit of fluid mass) is still held by the obstacle even at $t = 10$ s.

wider face), the maximum amount of debris bulk is held by the blunt face of the obstacle at $t = 4$ s. Due to the incoming debris flow, the pressure gradient, the size (geometry) of the obstacle and the gravity component along the slope, the blunt face can not withstand all of the debris bulk. The flow continues to leave from the lateral sides thereby decreasing the flow height in front of the obstacle after $t = 4$ s. Until $t = 9$ s, there is a large amount of debris mass accumulated on the front face of the tetrahedron even when there is no inflow of the debris material approaching the tetrahedron. At $t = 9$ s, the deflected debris mass is still flowing in two streams, while the two streams were already detached in case of the forward-facing tetrahedron. The relative maximum of the debris mass still lies in front of the blunt face, where the maxima were already in the run out zones in case of Fig. 4. At $t = 10$ s, a substantial amount of solid (also a bit of fluid) is still seen in front of the blunt face of the tetrahedron. Due to the solid fluid mixture and, mainly the obstacle induced guided flow with larger hydraulic pressure gradients in the downslope, the flow moves/travels efficiently farther in the run out region even after experiencing topographic change in the transition region.

The process of interaction and the subsequent mass flow is different in Fig. 5 than in Fig. 4. The main difference is that there is substantially larger deposition of mass, especially the solid, at the blunt face of the tetrahedron in Fig. 5. Moreover, the forward-facing tetrahedron deflects the debris wider than the rearward-facing tetrahedron due to its sharp faces that substantially and easily redirects the flow. Debris vacuum (Pudasaini, 2014) is created only at the backside of the tetrahedron in Fig. 4, whereas the debris vacuum is also seen at the lee side of the obstacle in Fig. 5. At each panel from $t = 4$ s to $t = 10$ s, the debris mass flows faster in case of the forward-facing tetrahedron than in case of the rearward-facing tetrahedron. The differences result from the difference in topographical gradients of the impacting faces of the tetrahedra. The rearward facing tetrahedron, is thus, a suitable dissipating structure in case there is not sufficient area of deposition in the run out zone as it arrests a portion of the debris material. Once the debris flow hits the obstacle, the deposited material may need its removal before another potential debris flow occurs in the same track (Gray et al., 2003; Pudasaini and Hutter, 2007). The forward-facing tetrahedra are more effective deflecting defense structures in case if there is sufficient space to divert the debris in the run out zone. If they are constructed higher on the slope, the deflection can be made wider so as to mitigate a larger area downstream.

3.3. Flow past integrated obstacles

Instead of mounting a larger obstacle, installing a number of smaller obstacles in the flow path is another way of mitigation by stabilizing the flow due to holding up of a portion of the mass and causing energy dissipation due to flow-obstacle-interaction. Smaller obstacles downstream can also redirect the flow in the desired direction (Johannesson et al., 2009; Teufelsbauer et al., 2009; Naaim et al., 2010; Teufelsbauer et al., 2011).

In this section, we present the interaction of the debris flows with multiple obstacles. The first obstacle is a forward-facing tetrahedron of the same size at the same location as in Fig. 4 which alters the main flow by deflecting it into two streams. The deflected streams are further impacted by two other tetrahedral obstacles of different sizes and orientations. In some cases, these two tetrahedra are kept almost in the flow lines, while in the other cases they are kept to divert the debris mass further in the flow lines, inward or outward. Such orientations further allow from strong to weak flow obstacle interactions and result in completely different flow dynamics, phase-separations and deposition behaviours.

(I) Flow past multiple obstacles in the flow lines

a. All three forward facing tetrahedra

In Fig. 6, the first tetrahedron on the slope has the same size, location and orientation as given in Fig. 4. The other two tetrahedra are smaller in size and are almost in the deflected flow lines oriented $\pm 8.13^\circ$ from the $y = 0$ line. These two tetrahedra have $(178, \pm 70, 0)$ m, $(212, \pm 54, 0)$ m and $(204, \pm 98, 0)$ m as the vertices of the triangular base, and the apices are at $(192, \pm 72, 15)$ m. The two downstream tetrahedra have smaller bases and are lower in heights as they are subjected to interact the debris flows with less mass divided into two halves due to the first tetrahedron. This is the reason for reducing their size and height by a factor of two. The flow dynamics and the obstacle interaction before $t = 6$ s are exactly the same with those presented in Fig. 4 as the deflected streams due to the first obstacle only impact the downstream obstacles nearly at $t = 6$ s. The two downstream obstacles begin to further divide the streams into two and deflect the streams by their sharp faces. At $t = 7$ s, the solid phase and the total debris bulk have their relative maxima in the vicinity of all three obstacles. In the case of fluid phase, the relative maxima are relatively longer and stretched along the streams and also at the obstacle fronts. After $t = 9$ s, the interaction of the flow by the first obstacle is almost complete. The two more obstacles locally further dissipate kinetic energy, and so the momentum is largely reduced. This can be seen at $t = 10$ s, when the frontal debris mixture reaches at $x = 250$ m but it was nearly at $x = 300$ m in Fig. 4. It may be more interesting to see the completely different obstacle interaction and the flow dynamics of solid and fluid from $t = 10$ s onward. Due to the flow diversion and energy or momentum loss in multiple obstacle interactions, the travel time is substantially longer in Fig. 6 as compared to Fig. 4 as indicated by the flow front in the respective figures. More solid mass is deflected outward and more fluid mass is deflected inward by both of these downstream obstacles. The inward streams travel more downslope than the outward streams. Thus tetrahedral obstacles may also play an important role for the phase-separation of the debris flow that mainly emerges here from the geometric contribution.

In the interaction of a two-phase flow with structure, (rapidly) changing basal surface may separate the fluid and the solid phases. Shearing or deformations of the solid and fluid may alter substantially when there is abrupt geometric change due to obstacle on the basal surface. So, topographic pressure gradient may have significant contribution to the phase-separation. Similarly, the different frictional behaviour of the two phases in a debris flow is also a cause of separation of phases. These and other causes of phase-separation have been explained in detail in Pudasaini and Fischer (2016b) by presenting a two-phase mechanical model for phase-separation in debris flow that introduces the separation-flux mechanism.

The simulated phase-separation by tetrahedra appears plausible. For the fluid phase, the material is mechanically weak and thus has been easily diverted in the preferential inward directions by the two downstream tetrahedra. This appears already from $t = 7$ s and intensifies for $t > 7$ s until all the fluid mass passes the obstacles. The nominal outward deflection of the fluid is due to the accumulation of the mixture mass that also holds some fluid, and the resulting outward motion is mainly due to the hydraulic pressure gradients in the lateral directions. However, for the solid, as the material is frictional, it can develop into a heap associated to internal and basal friction angles. This is seen from $t = 7$ s to $t = 10$ s for which the material more or less continuously piles up in the vicinity of the frontal nose of the tetrahedra with some downward motions as indicated by the four streams. The orientations of the tetrahedra preferentially develop higher lateral pressure gradients due to the higher amount of accumulation (rate) of the solid in the outer flanks of the two tetrahedra. This resulted in a substantially larger amount of solid particle flow along the outer flanks of the lower tetrahedra in the run out zone. In total, since the amount of solid in the initial material composition is substantially larger than the fluid, the run out patterns (fans) of the total debris mixture at $t = 13$ s have solid volume dominated outer flanks whereas the inner flanks contain a substantial amount of fluid. Since the fluid phase inner lobes are

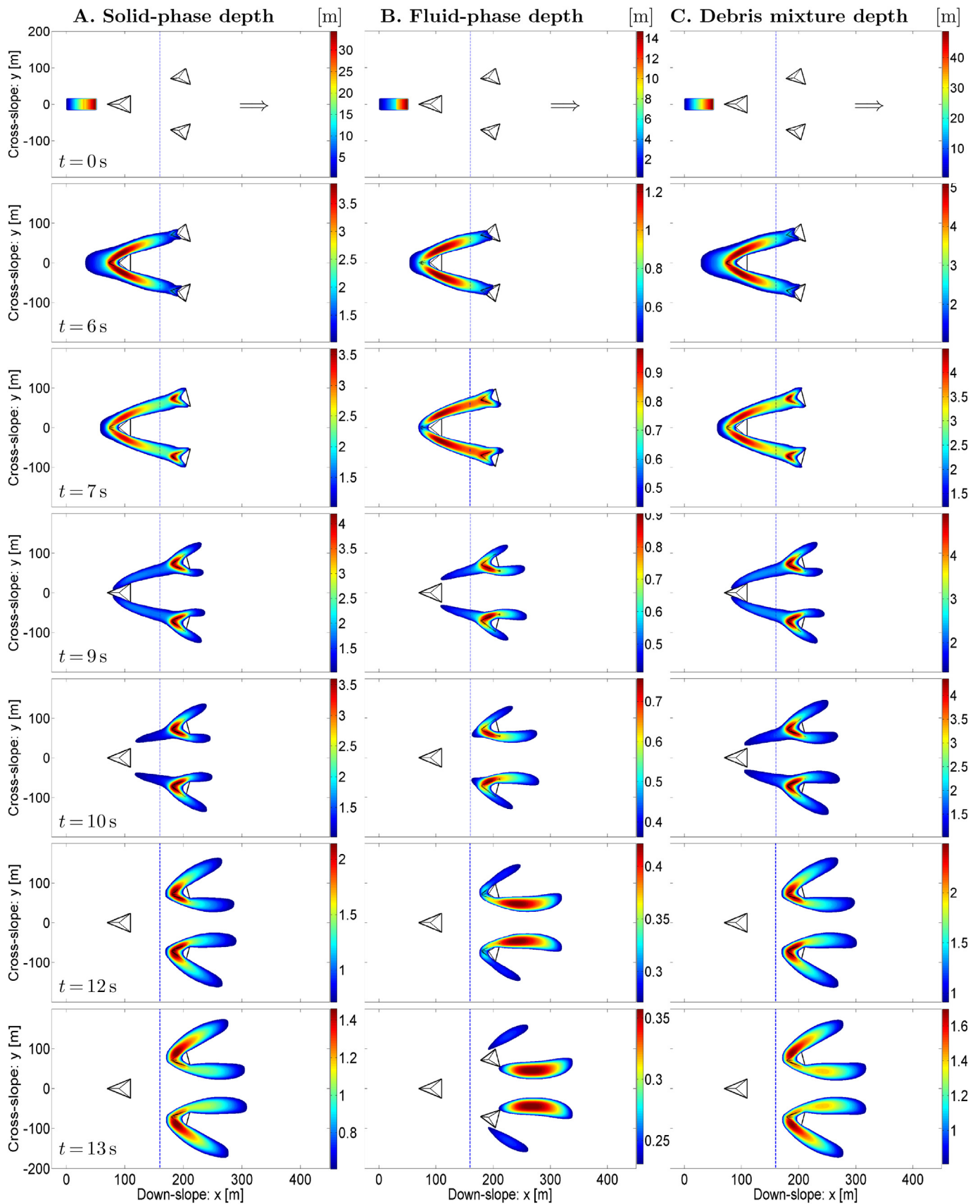


Fig. 6. Forward-facing tetrahedron followed by two forward-facing tetrahedra almost in the flow lines: Evolution and flow-obstacle-interaction of A. Solid phase, B. Fluid phase, C. Total debris mixture at $t = 0, 6, 7, 9, 10, 12$ and 13 s as a debris flow is triggered and hits a forward-facing tetrahedral obstacle followed by two more forward-facing tetrahedra in the flow lines. The arrows in the top panels indicate the flow direction. The blue dashed lines indicate the transition from the inclined plane to horizontal run out. The two debris streams deflected by the first tetrahedron are further deflected by the two smaller tetrahedra downstream showing multiple streamed lobes. More solid is obstructed and deflected outward, whereas more fluid is deflected inward, creating phase-separation.

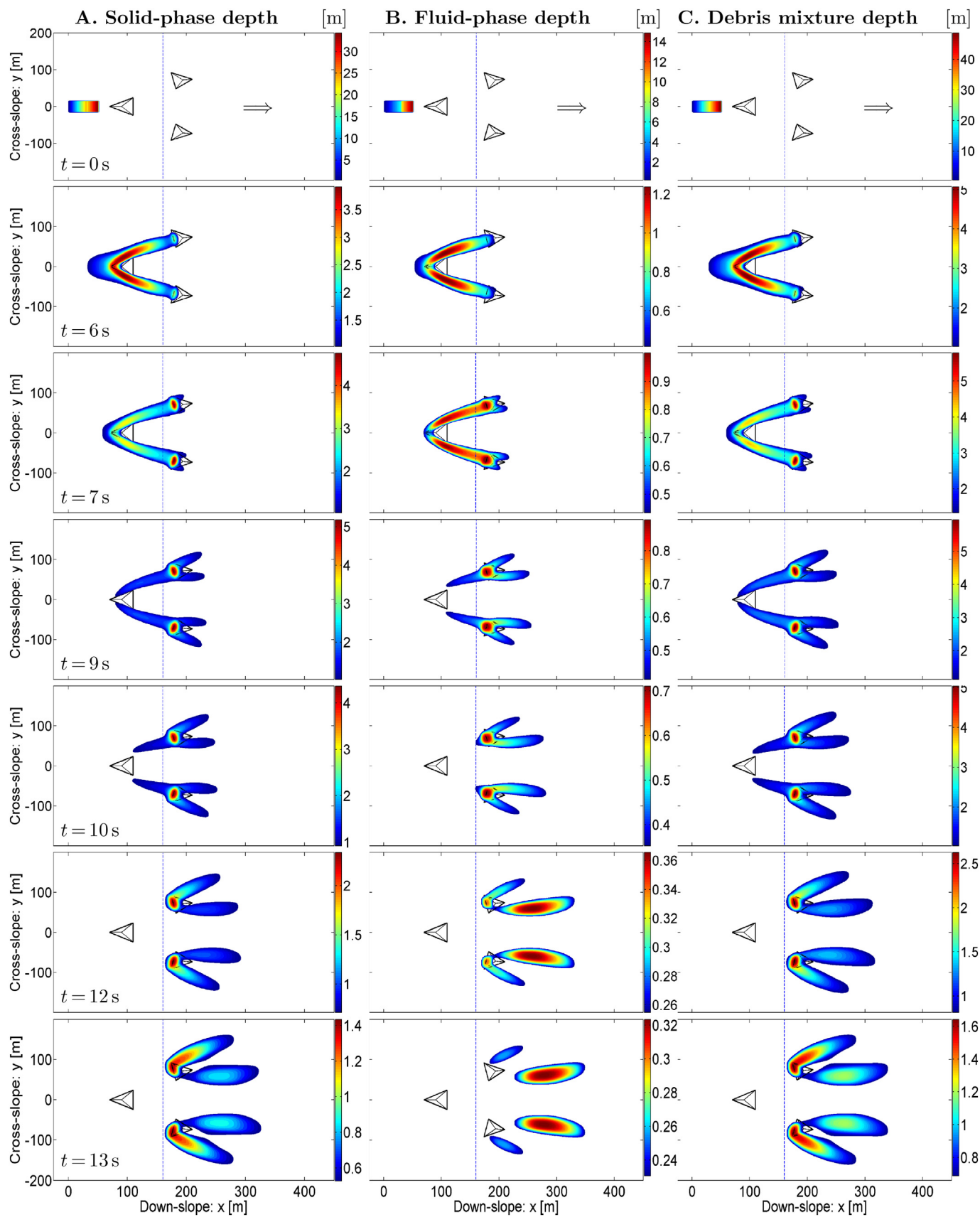


Fig. 7. Forward-facing tetrahedron followed by two rearward-facing tetrahedra almost in the flow lines. Evolution and flow-obstacle-interaction of A. Solid phase, B. Fluid phase, C. Total debris mixture at $t = 0, 6, 7, 9, 10, 12$ and 13 s as a debris flow is triggered and hits a forward-facing tetrahedral obstacle followed by two rearward-facing tetrahedra in the flow lines. The arrows in the top panels indicate the flow direction. The blue dashed lines indicate the transition from the inclined plane to horizontal run out. More solid mass is held by the obstacle than the fluid mass at $t = 13$ s. The two downstream tetrahedra deflect the debris mass narrower than in Fig. 6.

relatively wider, the final inner fans at $t = 13$ s are also wide.

This arrangement of tetrahedral obstacles, thus, has several advantages: (i) By energy dissipation, the run out time is longer, the run out length is shorter and the flow has less mobility, thereby making the flow less hazardous. (ii) By the impact vacuum behind the obstacles in the flow lines, the risk for the areas in the impact vacuum can be reduced. (iii) Due to the phase-separation, dense solid part of the debris can be diverted to the outer banks and more fluid can be diverted inward. In field events, this will occur as deposition of sand, gravel and boulders at the outer banks, which can be used commercially as construction materials. So, this type of arrangements of obstacles can be beneficial also from an economic point of view.

b. One forward-facing tetrahedron followed by two rearward-facing tetrahedra

In Fig. 7, the first forward facing tetrahedron is of same size and located at the same position as in the previous cases, but with two rearward facing tetrahedra mounted almost perpendicularly to the two deflected flow lines due to the first tetrahedron. The triangular base of the two downstream tetrahedra have the vertices at $(210, \pm 74, 0)$ m, $(174, \pm 92, 0)$ m and $(182, \pm 48, 0)$ m and the apices are at $(194, \pm 72, 15)$ m. Due to the blunt faces, these two downstream tetrahedra cause more obstruction to the flow for a while. This results in the increase in debris depths in front of these obstacles ($t = 7$ s to $t = 9$ s). As the front faces of these downstream tetrahedra are also inclined at an angle of 18.43° with the horizontal, they provide extra inward slopes to the flow and can not obstruct the flow completely. Due to friction, more solid and less fluid is held by the front faces of the downstream tetrahedra. It is again interesting to observe that more solid mass is deflected outward and more fluid mass is deflected inward. At $t = 13$ s, the inward deflected fluid streams are completely detached from the obstacles. The inward deflected streams travel farther downslope than the outward deflected streams as indicated by strongly outward curved lobes ($t = 12$ s, 13 s). The solid mass is more forcefully diverted outward by the tetrahedra. Due to the orientations of the lower tetrahedra, the flow obstacle interactions, mass diversion, motion and dispersion (or redirection) are substantially different now than in Fig. 6. Figure 7 shows that a small local difference in the dynamics of the front and its interaction with the obstacle, and the small positional deviation of the accumulations of the solid and fluid phases at the impacting front faces of the tetrahedra result in completely different scenarios. A careful scrutiny of solid and fluid panels at $t = 6$ s clearly reveal that the solid particles are accumulating just a bit outer portion of the front faces of the tetrahedra whereas the fluid is accumulating in just a bit inner portion of the same flanks. The reason for this is a minute difference in the frontal positions of impacting solid and fluid lobes. This results in the accumulation of more and more solid mass a bit in the outer part of the front face of the tetrahedron until $t = 9$ s with a little flow downslope. Then, due to impact direction, orientation of the flank, the locally developed pressure gradients, and the local position of the accumulated mass, the solid material moved outward resulting in a significant phase-separation. But, as the flank slope quickly decreases outward, it could not continuously push the solid mass further outward. In the mean time, the gravity pulls the mass in the downslope. This explains the strong surface curvature (or bending) of the solid phase mass flow. Similar behaviour for strong curving can be explained for the fluid but with the major portion of the material flowing in the inward lobes as in Fig. 6. Furthermore, due to the larger portion of the solid in the initial mixture, the dynamics of the total debris is similar to that of the solid phase.

(II) Flow past multiple obstacles with varied orientations

Until now, we have discussed the flow obstacle interactions and the subsequent flow dynamics in case when single and multiple obstacles

were mounted almost in the flow lines. In natural debris flows, the obstacles might be aligned with the flow lines. Sometimes, for the mitigation purpose, we may need to artificially construct the obstacles so as to arrest and/or redirect or deflect the debris flow in the desired directions. So, in the sequel, we present and discuss some of the simulation results related to flow obstacle interaction when the first forward-facing tetrahedron is of the same dimensions and located at the same place as in the previous cases, but the two downstream tetrahedra vary in size, location and orientation to study the subsequent effects.

a. Two more tetrahedra with inward-oblique impacting faces

In the simulation results presented in Fig. 8, the two downstream tetrahedra have the vertices of their bases at $(214, \pm 86, 0)$ m, $(172, \pm 110, 0)$ m, $(190, \pm 50, 0)$ m. The apices are at $(194, \pm 86, 15)$ m. At $t = 6$ s, the deflected debris streams due to the first forward-facing tetrahedron begin to impact the large inward-oblique faces of the two downstream tetrahedra. Due to friction, the major solid part is held by the front faces but the fluid part flows more smoothly ($t = 7$ s). From $t = 9$ s onward, even more interesting flow-obstacle-interaction can be seen. A bit of solid also begins to flow downstream but the fluid flow is substantial. At $t = 10$ s, while a large amount of solid mass is still held by the front face, most of the fluid mass has flown downstream. At $t = 12$ s, the obstruction of the solid mass by the front faces of the downstream tetrahedra still persists, but the major portion of the fluid mass already passes through the downstream tetrahedra. At $t = 13$ s, a substantial amount of solid mass is arrested by the tetrahedra. No fluid mass is arrested. The escaped solid and fluid masses are diverted inside, but due to their previous momenta, they tend to substantially divert away from the central line in the run out zone. Such orientations of the obstacles can be very useful for arresting the solid mass of the debris flow and make the flow less dense, facilitating irrigation or hydroelectric re-use of the particle-laden water. Although this arrangement of obstacles can mitigate a narrower area downstream around the central line ($y = 0$), a larger area in the outer banks can be mitigated.

The different flow obstacle interactions and the changing geometry of the solid and fluid phases in Fig. 8 can be explained. When the two deflected debris streams due to the first tetrahedron on the slope impact the front faces of the two downstream tetrahedra on the run out zone, these faces not only obstruct the flow for a while, but also provide extra slope to direct the flow inward (toward the central line, $y = 0$). Due to their previous momenta, the pressure developed due to the accumulation of the debris material and the inward slope of the faces, both the solid and fluid phases are directed inward. Due to the basal and the internal frictions of the solid material, and the loss of momentum due to the impact, a large portion of solid is deposited at the front faces of the two downstream tetrahedra.

b. Two more tetrahedra with straight impacting faces

In Fig. 9, the first forward facing tetrahedron has the same position and dimensions as before but the two downstream tetrahedra have their impacting faces perpendicular to the horizontal. So, these faces are inclined with the oblique flow lines due to the first forward-facing tetrahedron. The bases of the downstream tetrahedra have the vertices at $(210, \pm 72, 0)$ m, $(178, \pm 90, 0)$ m, $(178, \pm 46, 0)$ m. The apices are at $(194, \pm 70, 15)$ m. At $t = 6$ s, the two deflected debris streams due to the first forward-facing-tetrahedron begin to impact the straight faces of the two downstream tetrahedra. From $t = 7$ s to $t = 9$ s, the solid phase depth and total debris mixture depth have increased in front of the blunt faces of the downstream tetrahedra due to the obstruction. The upstream moving normal shocks are formed in front of these faces. Later, when there is a level of maximum accumulation, more pressure (normal load) is developed. Due to this, the mass starts flowing further downstream. Until $t = 10$ s, the solid, fluid and so the total debris bulk are obstructed quite a while, then are further deflected in multiple

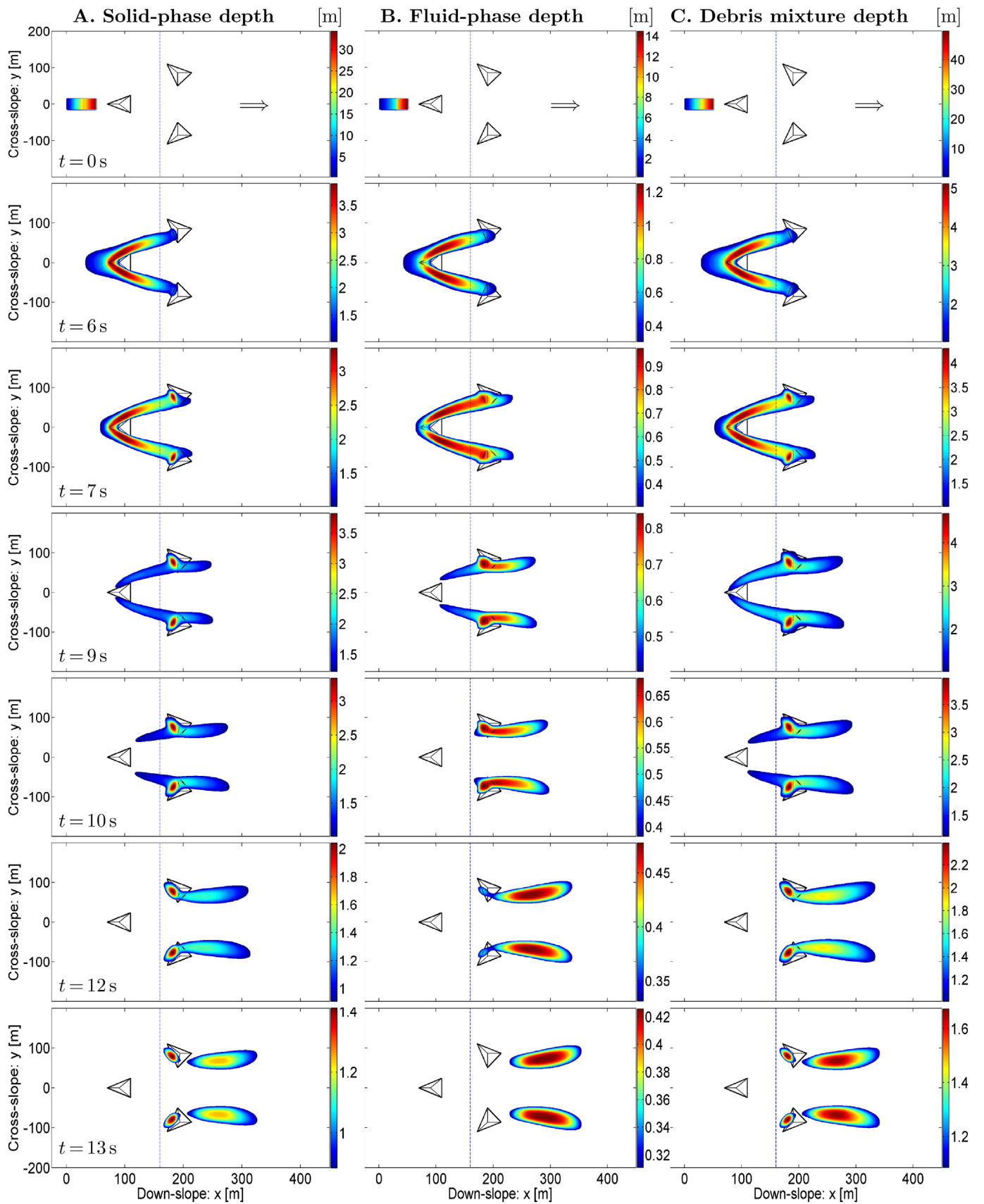


Fig. 8. Forward-facing tetrahedron followed by two inward-oblique tetrahedra. Evolution and flow-obstacle-interaction of A. Solid phase, B. Fluid phase, C. Total debris mixture at $t = 0, 6, 7, 9, 10, 12$ and 13 s as a debris flow is triggered and hits a forward-facing tetrahedral obstacle followed by two inward-oblique tetrahedra. The arrows in the top panels indicate the flow direction. The blue dashed lines indicate the transition from the inclined plane to horizontal run out. As the front faces of the downstream tetrahedra are inward oblique, no debris mass is deflected outward. A large amount of solid is arrested by the two downstream tetrahedra.

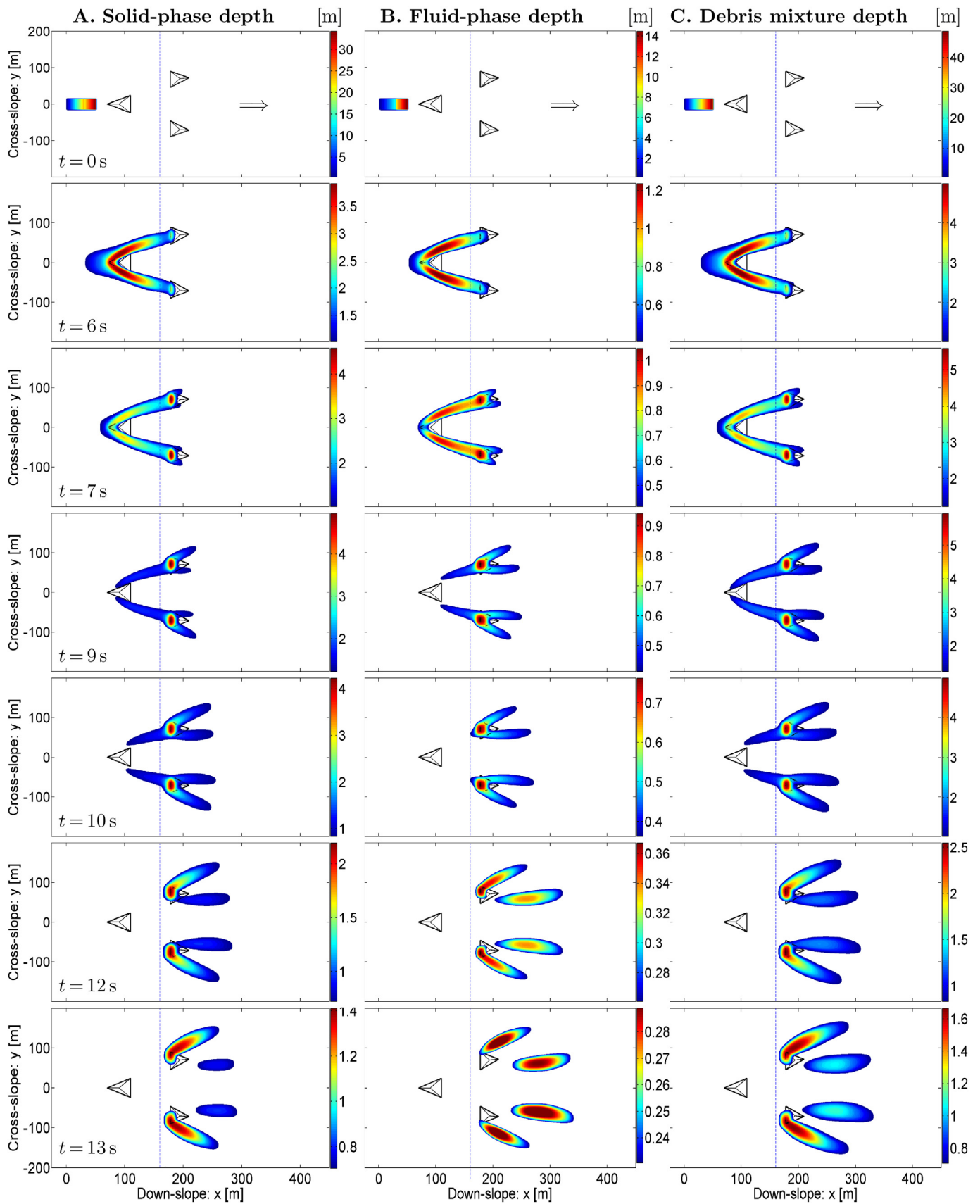


Fig. 9. Forward-facing tetrahedron followed by two straight rearward-facing tetrahedra. Evolution and flow-obstacle-interaction of A. Solid phase, B. Fluid phase, C. Total debris mixture at $t = 0, 6, 7, 9, 10, 12$ and 13 s as a debris flow is triggered and hits a forward-facing tetrahedral obstacle followed by two straight rearward-facing tetrahedra. The arrows in the top panels indicate the flow direction. The blue dashed lines indicate the transition from the inclined plane to horizontal run out. Major portion of the solid part is obstructed and deflected in outward direction. The fluid part is almost equally divided into four steamed lobes: two in outward and the other two in inward directions. The inward deflected debris bulk contains almost all fluid.

streamlines. The obstruction, deflection and advection of solid, fluid and total debris bulk continue until $t = 12$ s. However, the inward directed fluid lobes are already detached from the downstream tetrahedra and travel more downslope than the solid lobes and the other two fluid lobes are deflected in outward direction. Since a very large amount (almost all) of the solid mass is strongly deflected away from the main flow path, the impact in this region has tremendously been reduced by installing the obstacles as arranged here.

The different flow-obstacle-interactions of solid and fluid phases arise when the flow begins to hit the front straight faces of the two downstream tetrahedra, at $t = 6$ s. At $t = 7$ s, as the relative maxima of solid lie at the front of the impacting faces and fluid has long tails of maxima, the difference in their dynamical interactions with the obstacles is more pronounced. Due to the internal and basal friction angles, the accumulation of solid at the front of the obstacles increases as it piles up. Pressure is more developed due to this accumulation resulting in the deflection of substantial solid mass in outward direction, following its previous momenta. As the obstructed and flowing solid mass in outward direction, to some extent, hinders the flow of fluid in outer direction, considerable amount of fluid flows in inward direction ($t \geq 10$ s). This is because, the fluid part is mechanically weaker than the solid part. At $t = 12$ s, more solid than fluid is held by the obstacles in outward direction. Due to this, the deflected debris lobes in outward direction moves less downslope than the inward deflected debris lobes. At $t = 13$ s, the solid obstruction still persists in the outward direction, but the fluid part is already about to detach from the outer edges of the downstream tetrahedra.

The flow obstacle interaction and the subsequent flow dynamics in Fig. 9 is more similar to those in Fig. 7. However, at $t = 13$ s, the fluid phase is almost equally divided into four lobes, two outward and two inward, and almost all the solid is deflected outward. The case was different in Fig. 7: more fluid was directed inward and a small amount of fluid was deflected outward. To sum up, the straight orientations of the two downstream tetrahedra cause the huge loss of solid momentum, giving rise to a significant mitigation in downslope direction.

c. Two more tetrahedra with outward-oblique impacting faces

In Fig. 10 also, we have not changed the position and dimensions of the first forward-facing tetrahedron. Two outward-oblique tetrahedra are arranged in the run out zone so as to divert the flow farther away from the central line ($y = 0$). These two outward oblique tetrahedra have the vertices of the base at $(214, \pm 62, 0)$ m, $(186, \pm 80, 0)$ m, $(178, \pm 32, 0)$ m. Their apices are at $(198, \pm 58, 15)$ m. At $t = 6$ s, the deflected solid, fluid and total debris streams begin to hit the frontal oblique faces of the lower tetrahedra. As the faces are sloped outward, the two flowing streams are diverted outward and no portion is diverted inward. The front faces of the two downstream tetrahedra begin to impact the two debris streams deflected by the first tetrahedron on the slope. As the front faces of the downstream tetrahedra are outward oblique, they redirect the flow in the outward direction. This process continues as time progresses. The front faces give more obstruction to the solid (being frictional material) in comparison to fluid. At $t = 10$ s, solid part of the deflected debris streams from the first tetrahedron is still impinging on the oblique faces of the two tetrahedra, whereas all the fluid part has already hit the frontal blunt face and a substantial part has already been deflected away. By $t = 13$ s, there is still substantial solid part in the outer sides of the obstacles, but the fluid part has already been deflected away from the obstacles. Since the impact causes both the solid and fluid to deflect more in cross slope direction along with more obstruction of the solid part, there is less advection of the major solid part of the debris bulk in the cross slope direction. In the inundation area, the debris will have sudden strong impact of the flow front, but with less dynamic pressure of the debris body. Such placing of obstacles is very useful to deflect away the fluid part and to hold or deflect away the solid part from the central region. As the deflected

streams are wider apart in comparison to the previous cases and no part of the debris bulk is deflected inward, this type of arrangements of obstacles can mitigate a wider area downstream, keeping the region in between relatively safe from the debris flow hazard.

4. Comparison with dry granular flows interacting with obstacles

Here, we summarize some important phenomena observed in dry granular flows interacting with obstacles in experiments by Hákonardóttir et al. (2003a, 2003b, 2003c), Hákonardóttir (2004) and Faug (2015) relevant to this study. We discuss some plausible similarities and differences between these flows and the flows of mixture of viscous fluid and granular materials in connection to flow-obstacle-interactions.

Hákonardóttir et al. (2003a) reported a novel experimental study of the interaction of a rapid granular flow with a solid barrier (dam). Dam height to the flow ratio (H/h) was as high as 5. The barriers had a planar upstream face, which was inclined at relatively high angles (30° - 90°) and spanned the width of the rectangular chute. A relatively loose dry granular material (small glass particles), with volume fractions of 0.3–0.5 was used. Their experiments show that on reaching the dam, the stream of particles was projected from the top of the dam and formed an airborne coherent inviscid granular jet as it detaches from the top of the obstacle, that later landed on the chute with a ballistic trajectory. Hákonardóttir et al. (2003b) conducted further laboratory experiments in a long chute, with changing slope angle, to investigate the interaction of a supercritical granular flow with obstacles. A row of mounds were mounted in the transition zone to the run out and were typically inclined at 90° with the channel slope. The collision of the flow with these obstacles led to the formation of a jet. They suggested that a row of steep mounds, with an elongated shape in the transverse direction to the flow and with a height several times the flow depth, led to dissipation of a large proportion of the flow kinetic energy. Moreover, Hákonardóttir et al. (2003c) performed large-scale experiments to study the interaction of a snow avalanche with a row of mounds. The angle between the upstream face of the mounds and the experimental chute was 90° . As in Hákonardóttir et al. (2003a, 2003b), the avalanche in these experiments detached from the top of the mound and formed a coherent airborne jet. Those physical, mechanical and geometrical conditions associated with experiments in Hákonardóttir et al. (2003a, 2003b, 2003c) were probably favourable in generating flying granular jets as the supercritical flows impacted the rigid barriers. However, the debris flow-obstacle-interactions considered here may not meet all, or most of these conditions.

Figure 11 plots the ratio of the obstacle height to the incoming debris flow depth (H/h) versus incoming flow Froude number ($Fr = u/\sqrt{gh \cos \zeta}$) for (A) forward-facing pyramid, and (B) rearward-facing pyramid for $t > 2$ to $t = 4$ s corresponding to Figs. 4 and 5 respectively. In both cases, with increasing Fr , H/h decreases first and increases rapidly in Fig. 11A, whereas remains almost constant in Fig. 11B for some range of Fr . This is due to the different geometry of the faces of the obstacles with which the flow interacts. In fact, the rearward-facing pyramid momentarily holds more debris mass than the forward-facing pyramid during the obstacle-interaction. Later, H/h increases more rapidly in Fig. 11B than in Fig. 11A. As the width of the obstacles are much smaller as compared to the channel width, the debris mass flow from the lateral flanks of the obstacles without reaching the flow boundary far in the lateral direction. Faug (2015) proposed a phase-diagram (H/h vs. Fr) employing the depth-averaged analytic solutions for free surface granular flows impacting rigid walls down inclines. The diagram shows that airborne jets are formed for $Fr > 4$ and $1 < H/h < 14$. In our numerical experiments, Fr is not significantly greater than 4. This may indicate for not forming debris jets in our simulations. Moreover, in the experiments performed by Gray et al. (2003), when the granular flow impacts the forward- and

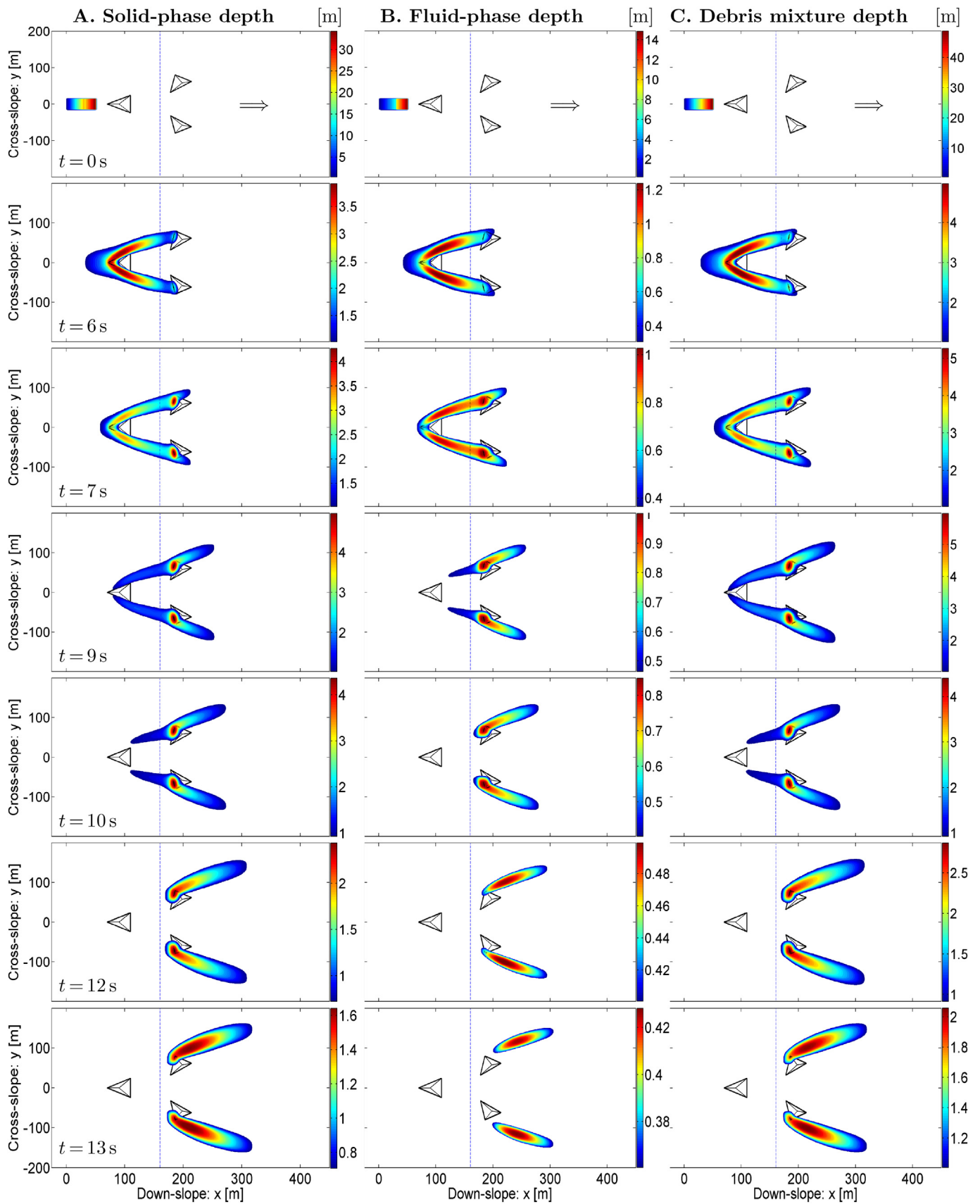


Fig. 10. Forward-facing tetrahedron followed by two outward-oblique rearward-facing tetrahedra. Evolution and flow-obstacle-interaction of A. Solid phase, B. Fluid phase, C. Total debris mixture at $t = 0, 6, 7, 9, 10, 12$ and 13 s as a debris flow is triggered and hits a forward-facing tetrahedral obstacle followed by two outward-oblique rearward-facing tetrahedra. The arrows in the top panels indicate the flow direction. The blue dashed lines indicate the transition from the inclined plane to horizontal run out. The two downstream tetrahedra hold a portion of solid and no debris mass is deflected inward. There is wider deflection in cross-stream direction as compared to the previous cases.

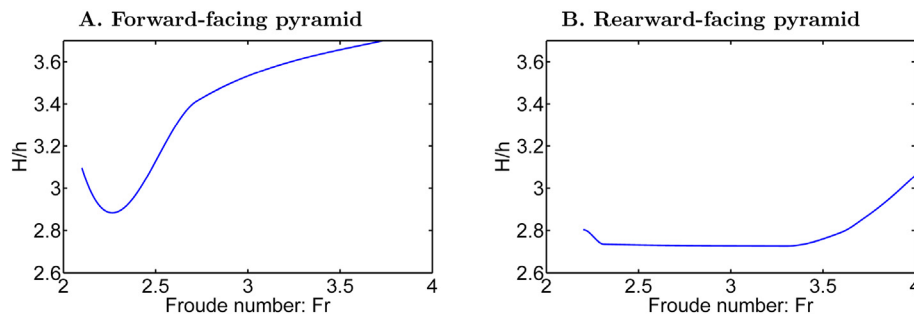


Fig. 11. Ratio of obstacle height to the incoming debris flow depth (H/h) versus incoming flow Froude number (Fr) for A: the forward facing pyramid (Fig. 4), and B: the rearward-facing pyramid (Fig. 5).

rearward-facing pyramids, Fr were 5.79–5.86. In their experiments oblique and upstream shocks were formed, but the granular jets were not formed as in our results.

However, there are some more reasons for not forming debris jets in our numerical experiments. First of all, the flow mechanics may play a role. In contrast to the dry and loose granular material, the debris mixture, consisting of granular particles and the viscous fluid, can behave fundamentally differently and may, to some extent, prevent from forming a similar debris jet. Nevertheless, in the limit, if the mixture is very dilute (much less amount of particles), the jets may still be formed. In other spectrum of the limit, if the mixture consists of very small fraction of fluid such that the momentum transfer in the mixture is not substantially influenced by the fluid fraction, the material may behave as if it was a dry material (Pudasaini and Hutter, 2007). Our mixture material typically consists of 75% of solid and 25% of fluid, and both the granular friction and the fluid viscosity play important role that generally controls the material from approaching the limit of the dry and fluid flows. Thus, the flow is characteristically a dense mixture flow. So, the formation of debris jets of that extent discussed in the previous paragraph is less likely. Second, the geometrical configuration may even play the dominant role. In the experiments by Hákonardóttir et al. (2003a, 2003b, 2003c), the obstacles spanned in the transversal direction, covering fully or mostly the rectangular channel (for the case of a row of mounds). The base lines of the obstacles were aligned in the transversal direction. Even more significant aspect is that the angle between the upstream face of the dams and the chute was large. These constraints resulted in keeping the flow in the (narrow) rectangular channel without lateral spreading (or, much less), and very quickly to abruptly changing the flow direction from the channel to the front surface of the obstacle that later developed into the flying jet. The geometrical conditions in the present study are different in which the flow takes place in the laterally wide channel such that it can freely spread transversally before it impacts the obstacles. Another crucial aspect is that we used tetrahedral pyramids whose flanks are obliquely aligned to the lateral direction and are inclined to relatively gentle angles with the channel surface. So, although the flow obstacle interaction in the present study is strong, it is less abrupt than in the experiments by Hákonardóttir et al. (2003a, 2003b, 2003c) and Faug (2015). This prevented from forming the debris jets. The third aspect is that unlike in the experiments of Hákonardóttir et al. (2003a, 2003b, 2003c) and Faug (2015), the debris flows in our simulations virtually did not overtop the peak of the pyramids but only spread on the relatively gentle oblique lateral flanks. This also prevented the debris jet formation.

Interactions of granular flows with smoothly changing obstacles (or, topography) have been studied numerically (Greve and Hutter, 1993; Pudasaini and Hutter, 2007; Viroulet et al., 2017) that should also be extended for the debris mixture that may significantly increase the complexity. Here, due to the typical channel and obstacle geometries, we assume that the flow remains in contact with the sliding surface. However, a detailed investigation is required to identify which of these

mechanical, geometrical and configurational aspects play dominant role, how and in which order, in generating or not generating debris jets. So, the results presented here are subject to scrutiny with experimental data. Although this is not within the scope here, this important aspect should be dealt with in other contributions.

Furthermore, a large wall perpendicular to the basal surface could be more interesting in simulating impact pressure and catching the entire mass in the run out zone (Pudasaini et al., 2007). Here, we do not include this, because, this would prevent us from studying different solid and fluid flow dynamics around the obstacle and downstream.

Here, we mainly focused on the geometrical part of the flow-obstacle-interactions and some related aspects of reduced kinetic energy or momentum loss and reduced mass mobility. In some situations, as the flow was diverted on either sides of the flanks of the obstacle, the flow was channelized, spreading was controlled and the pressure developed in that region. This resulted in some plausible enhanced travel distance. However, we have presented only the qualitative pictures. Nevertheless, the detailed and quantitative analysis of dynamical aspects about the reduced kinetic energy, momentum loss and reduced mass mobility due to flow channeling and pressure build-up will be presented in some other contributions to follow.

5. Conclusions

Here, we presented and discussed some basic simulation results for two-phase mass flows on a generic topography, interacting with tetrahedral obstacles. The different sets of simulations include the obstacles of different sizes, locations, numbers, orientations and spacing in the flow region.

Through the simulations, fundamentally different interacting behaviours of the solid and fluid phases with different obstacles have been identified. A forward facing tetrahedron constructed on the upper part of the surface can protect a larger area by deflecting the debris flow with wider debris vacuum. A rearward-facing tetrahedron can be used to substantially arrest the debris mass in its vicinity and let a reduced portion of the debris volume to run out. Different other obstacles can be constructed downstream to further catch or divert the debris mass in the desired direction when required. Although each obstacle constellation is more or less responsible for the phase-separation (between the solid and fluid phases) by redirecting different amount of solid and fluid mass in different directions, phase-separation is more pronounced in some suitable arrangements of the obstacles. Significant separation of solid and fluid phases generally produced by the interaction of the debris mixture with the integrated obstacles, opens a new path to future experimental studies to be designed and conducted. We also found that the dynamic impact pressure computed from the density and the velocity of the debris mixture is considerably lower than mechanically more appropriate barycentric impact pressure computed from the solid- and fluid-phases pressures. Our analysis of the ratio of the obstacle height to the flow depth with the incoming flow Froude number explains the reason for not forming debris jets in our numerical

experiments.

The simulations reveal that properly designed and suitably placed obstacles in the course of debris flows can be used in the mitigation process by catching the debris mass and/or deflecting it away from potential areas at risk. With respect to the real two-phase modelling and simulations, these are novel results in describing the flow-obstacle interactions. This may help to planners and policy makers to develop evacuation plans and mitigation strategies in debris flow-, and GLOF (glacial lake outburst flood)-prone areas in mountains and valleys. Depending upon the anticipated volume of the debris, channel topography and the nature of the objects or the area to be protected, the real two-phase mass flow model and the simulation strategies adopted here can be further extended and applied to a wide range of gravitational mass flows, including granular flows, snow and rock avalanches, industrial mass flows as well as debris flows in torrents and flash floods impinging on the obstacles on their way. This forms a basis for advanced hazard mitigation planning and enhancement of safety measures against potential geo-disasters. These simulation results are yet to

be empirically confirmed by the field data of the past debris flow events or by laboratory experiments. However, this is not within the scope here.

Acknowledgements

Parameshwari Kattel acknowledges University Grants Commission (UGC), Nepal for the financial support provided as a PhD fellowship (PhD-2071/072-Sci. & Tech.-03). We gratefully acknowledge the financial support provided by the German Research Foundation (DFG) through the research projects, PU 386/5-1: “A novel and unified solution to multi-phase mass flows”: U^{MultiSol} ; and PU 386/3-1: “Development of a GIS-based Open Source Simulation Tool for Modelling General Avalanche and Debris Flows over Natural Topography”, and the Austrian Science Fund (FWF) through the research project I1600-N30: “A GIS simulation model for avalanche and debris flows” within a transnational research programme, D-A-CH.

Appendix A. The two-phase model equations

In a two-phase debris flow model (Pudasaini, 2012), the solid phase is characterized by its material density ρ_s , internal friction angle ϕ , basal friction angle δ , an anisotropic stress distribution, and the lateral earth pressure coefficients K_x and K_y , whereas the fluid phase is characterized by its material density ρ_f , viscosity η_f and an isotropic stress distribution. The subscripts s and f are for the solid and fluid phases, and x and y are for the downslope and cross slope directions respectively. The flow depth h , volume fraction of the fluid α_f (or the solid $\alpha_s = 1 - \alpha_f$), the depth-averaged velocity components for fluid $\mathbf{u}_f = (u_f, v_f)$ and for solid $\mathbf{u}_s = (u_s, v_s)$, in the downslope and the cross slope directions respectively, are to be computed as functions of space and time. The simulations are based on the following depth-averaged two-phase debris flow model by Pudasaini (2012).

$$\frac{\partial}{\partial t}(\alpha_s h) + \frac{\partial}{\partial x}(\alpha_s h u_s) + \frac{\partial}{\partial y}(\alpha_s h v_s) = 0, \tag{1}$$

$$\frac{\partial}{\partial t}(\alpha_f h) + \frac{\partial}{\partial x}(\alpha_f h u_f) + \frac{\partial}{\partial y}(\alpha_f h v_f) = 0, \tag{2}$$

$$\begin{aligned} &\frac{\partial}{\partial t}[\alpha_s h(u_s - \gamma \mathcal{C}(u_f - u_s))] + \frac{\partial}{\partial x} \left[\alpha_s h \left(u_s^2 - \gamma \mathcal{C}(u_f^2 - u_s^2) + \frac{\beta_{x_s} h}{2} \right) \right] \\ &+ \frac{\partial}{\partial y}[\alpha_s h(u_s v_s - \gamma \mathcal{C}(u_f v_f - u_s v_s))] = h S_{x_s}, \end{aligned} \tag{3}$$

$$\begin{aligned} &\frac{\partial}{\partial t}[\alpha_s h(v_s - \gamma \mathcal{C}(v_f - v_s))] + \frac{\partial}{\partial x}[\alpha_s h(u_s v_s - \gamma \mathcal{C}(u_f v_f - u_s v_s))] \\ &+ \frac{\partial}{\partial y} \left[\alpha_s h \left(v_s^2 - \gamma \mathcal{C}(v_f^2 - v_s^2) + \frac{\beta_{y_s} h}{2} \right) \right] = h S_{y_s}, \end{aligned} \tag{4}$$

$$\begin{aligned} &\frac{\partial}{\partial t} \left[\alpha_f h \left(u_f + \frac{\alpha_s}{\alpha_f} \mathcal{C}(u_f - u_s) \right) \right] + \frac{\partial}{\partial x} \left[\alpha_f h \left(u_f^2 + \frac{\alpha_s}{\alpha_f} \mathcal{C}(u_f^2 - u_s^2) + \frac{\beta_{x_f} h}{2} \right) \right] \\ &+ \frac{\partial}{\partial y} \left[\alpha_f h \left(u_f v_f + \frac{\alpha_s}{\alpha_f} \mathcal{C}(u_f v_f - u_s v_s) \right) \right] = h S_{x_f}, \end{aligned} \tag{5}$$

$$\begin{aligned} &\frac{\partial}{\partial t} \left[\alpha_f h \left(v_f + \frac{\alpha_s}{\alpha_f} \mathcal{C}(v_f - v_s) \right) \right] + \frac{\partial}{\partial x} \left[\alpha_f h \left(u_f v_f + \frac{\alpha_s}{\alpha_f} \mathcal{C}(u_f v_f - u_s v_s) \right) \right] \\ &+ \frac{\partial}{\partial y} \left[\alpha_f h \left(v_f^2 + \frac{\alpha_s}{\alpha_f} \mathcal{C}(v_f^2 - v_s^2) + \frac{\beta_{y_f} h}{2} \right) \right] = h S_{y_f}, \end{aligned} \tag{6}$$

where the pressures are given by

$$\beta_{x_s} = \varepsilon K_x p_{b_s}, \beta_{y_s} = \varepsilon K_y p_{b_s}, \beta_{x_f} = \beta_{y_f} = \varepsilon p_{b_f}, p_{b_f} = -g^z, p_{b_s} = (1 - \gamma) p_{b_f}.$$

Equations (1)–(2) are the depth-averaged mass balance equations for solid and fluid phases respectively. The last four equations are the depth-averaged momentum balances for solid (3)–(4) and fluid (5)–(6) in the x - and y -directions respectively. The source terms are (Pudasaini, 2012):

$$S_{x_s} = \alpha_s \left[g^x - p_{b_s} \left(\frac{u_s}{|\mathbf{u}_s|} \tan \delta + \varepsilon \frac{\partial b}{\partial x} \right) \right] - \varepsilon \alpha_s \gamma p_{b_f} \left[\frac{\partial h}{\partial x} + \frac{\partial b}{\partial x} \right] + C_{DG} (u_f - u_s) |\mathbf{u}_f - \mathbf{u}_s|^{J-1}, \tag{7}$$

$$S_{y_s} = \alpha_s \left[g^y - p_{bs} \left(\frac{v_s}{|\mathbf{u}_s|} \tan \delta + \varepsilon \frac{\partial b}{\partial y} \right) \right] - \varepsilon \alpha_s \gamma p_{bf} \left[\frac{\partial h}{\partial y} + \frac{\partial b}{\partial y} \right] + C_{DG} (v_f - v_s) |\mathbf{u}_f - \mathbf{u}_s|^{J-1}, \tag{8}$$

$$S_{x_f} = \alpha_f \left[g^x - \varepsilon \left[\frac{1}{2} p_{bf} \frac{h}{\alpha_f} \frac{\partial \alpha_s}{\partial x} + p_{bf} \frac{\partial b}{\partial x} - \frac{1}{\alpha_f N_R} \left(2 \frac{\partial^2 u_f}{\partial x^2} + \frac{\partial^2 v_f}{\partial y \partial x} + \frac{\partial^2 u_f}{\partial y^2} - \frac{\chi u_f}{\varepsilon^2 h^2} \right) \right] \right. \\ \left. + \frac{1}{\alpha_f N_{R_{\mathcal{A}}}} \left[2 \frac{\partial}{\partial x} \left(\frac{\partial \alpha_s}{\partial x} (u_f - u_s) \right) + \frac{\partial}{\partial y} \left(\frac{\partial \alpha_s}{\partial x} (v_f - v_s) + \frac{\partial \alpha_s}{\partial y} (u_f - u_s) \right) \right] - \frac{\xi \alpha_s (u_f - u_s)}{\varepsilon^2 \alpha_f N_{R_{\mathcal{A}}} h^2} \right] - \frac{1}{\gamma} C_{DG} (u_f - u_s) |\mathbf{u}_f - \mathbf{u}_s|^{J-1}, \tag{9}$$

$$S_{y_f} = \alpha_f \left[g^y - \varepsilon \left[\frac{1}{2} p_{bf} \frac{h}{\alpha_f} \frac{\partial \alpha_s}{\partial y} + p_{bf} \frac{\partial b}{\partial y} - \frac{1}{\alpha_f N_R} \left(2 \frac{\partial^2 v_f}{\partial y^2} + \frac{\partial^2 u_f}{\partial x \partial y} + \frac{\partial^2 v_f}{\partial x^2} - \frac{\chi v_f}{\varepsilon^2 h^2} \right) \right] \right. \\ \left. + \frac{1}{\alpha_f N_{R_{\mathcal{A}}}} \left[2 \frac{\partial}{\partial y} \left(\frac{\partial \alpha_s}{\partial y} (v_f - v_s) \right) + \frac{\partial}{\partial x} \left(\frac{\partial \alpha_s}{\partial y} (u_f - u_s) + \frac{\partial \alpha_s}{\partial x} (v_f - v_s) \right) \right] - \frac{\xi \alpha_s (v_f - v_s)}{\varepsilon^2 \alpha_f N_{R_{\mathcal{A}}} h^2} \right] - \frac{1}{\gamma} C_{DG} (v_f - v_s) |\mathbf{u}_f - \mathbf{u}_s|^{J-1}, \tag{10}$$

where the parameters are

$$C_{DG} = \frac{\alpha_s \alpha_f (1 - \gamma)}{[\varepsilon \mathcal{U}_T \{ \mathcal{F} \mathcal{F}(Re_p) + (1 - \mathcal{F}) \mathcal{F}(Re_p) \}]^J}, \gamma = \frac{\rho_f}{\rho_s}, \mathcal{F} = \frac{\gamma}{180} \left(\frac{\alpha_f}{\alpha_s} \right)^3 Re_p, \mathcal{G} = \alpha_f^{M(Re_p)-1}, Re_p = \frac{\rho_f d \mathcal{U}_T}{\eta_f}, N_R = \frac{\sqrt{gL} H \rho_f}{\alpha_f \eta_f}, N_{R_{\mathcal{A}}} = \frac{\sqrt{gL} H \rho_f}{\mathcal{A} \eta_f}. \tag{11}$$

In Eqs. (1)–(11), x, y and z refer the coordinates along the downslope direction, cross-wise direction and the direction perpendicular to the flow surface respectively and g^x, g^y and g^z are the respective components of acceleration due to gravity. $\varepsilon = H/L$ is the aspect ratio, where L and H are the typical extent and depth of the flow. $\mu = \tan \delta$ is the basal friction coefficient. C_{DG} is the generalized drag coefficient; $J = 1$ or 2 represents linear (laminar-type) or quadratic (turbulent-type) drag. \mathcal{U}_T is the terminal velocity of a particle and \mathcal{F} , which takes values within 0 and 1, is a parameter that combines the solid-like (\mathcal{G}) and fluid-like (\mathcal{F}) drag contributions to flow resistance. p_{bf} and p_b are the effective fluid and solid pressures. γ is the ratio of the density of the fluid phase to that of the solid phase, \mathcal{G} is the virtual mass coefficient, M is a function of the particle Reynolds number (Re_p), χ includes vertical shearing of fluid velocity, and ξ takes into account different distributions of α_s . $\mathcal{A} = \mathcal{A}(\alpha_f)$ is the mobility of the fluid at the interface. N_R is a quasi-Reynolds number and $N_{R_{\mathcal{A}}}$ a mobility-Reynolds number associated with the classical Newtonian and enhanced non-Newtonian fluid viscous stresses respectively. As input, we consider the basal and obstacle topography $z = b(x, y)$, along with the aforementioned material parameters, and initial and boundary conditions (see, Section 2) so that Eqs. (1)–(6) give output as debris flow depth h , volume fraction of the fluid α_f (or solid α_s) or equivalently, solid- and fluid-phase depths ($h_s = \alpha_s h, h_f = \alpha_f h$) and the depth-averaged velocity components for solid u_s and v_s , and for fluid u_f and v_f in the downslope and the cross wise directions respectively, as functions of space and time.

Appendix B. Description of impact pressure

Impact pressure of a debris flow can be categorized into (i) the sudden impact of the debris flow head (strong and rapid), (ii) continuous dynamic pressure of the debris body (steady), and (iii) static pressure of the debris tail (slight, can be neglected) (Cui et al., 2015). In a quasi static flow or in a hydrostatic model, the maximum debris flow pressure (p_H) on an obstacle is computed as (Armanini, 1997; Sovilla et al., 2016)

$$p_H = k \rho_m g h, \tag{12}$$

where k is an empirical factor depending on the dynamic behavior of the debris flow, ρ_m is the mixture density and h is the total depth of the debris mixture. The hydrodynamic model for rigid obstacles computes the dynamic pressure (p_D) of the debris flow as (Johannesson et al., 2009; Cui et al., 2015)

$$p_D = C_0 \rho_m v_m^2, \tag{13}$$

where v_m is the velocity of the debris mixture. In fact, in (13), C_0 is a factor describing the influence of the shape of the obstacle and generally taken to be 0.5. However, different authors (Hung et al., 1984; Zhang, 1993; Armanini, 1997; Bugnion et al., 2011; Cui et al., 2015; Vagnon and Segalini, 2016) have used the value of C_0 differently (0.4–10). There can be a lot of uncertainties in calculating the pressure of the debris flow impacting a structure (Gauer et al., 2008; Ancy and Bain, 2015). The case of debris flow hitting an obstacle at some angle is still very poorly understood. It is very difficult to estimate the actual area of the obstacle that is hit by the debris during the flow. So, we generally estimate the dynamic impact pressure by (Johannesson et al., 2009; Bovet, 2012; Cui et al., 2015; Sovilla et al., 2016)

$$p_D = \rho_m v_m^2 \sin^2 \theta \tag{14}$$

where θ is the acute angle between the direction of the debris flow velocity and the surface of the obstacle that is impacted. In (14), $\sin^2 \theta$ arises because in (13), we replace v_m by its component ($v_m \sin \theta$) in the direction of impact with the upstream surface of the obstacle from the normal direction. The parameters and variables involved in (14) are associated with the debris bulk that are specified and computed in Section 3.2a.

References

Ancy, C., Bain, V., 2015. Dynamics of glide avalanches and snow gliding. *Rev. Geophys.* 53 (3), 745–784. <http://dx.doi.org/10.1002/2015RG000491>.
 Armanini, A., 1997. On the dynamic impact of debris flows. In: *Recent Development of Debris Flows*. Springer, Berlin.
 Bagnold, R.A., 1954. Experiments on a gravity-free dispersion of large solid spheres in a Newtonian fluid under shear. *Proc. R. Soc. Lond., Ser. A* 225, 49–63.
 Bovet, E., 2012. *Mechanics of Snow Avalanches and Interaction With Structures*.

Politechnic of Turin <http://dx.doi.org/10.6092/polito/porto/2518989>. (PhD Thesis).
 Bugnion, L., McArdell, B.W., Bartelt, P., Wendeler, C., 2011. Measurements of hillslope debris flow impact pressures on obstacles. *Landslides* 9, 179–187. <http://dx.doi.org/10.1007/s10346-011-0294-4>.
 Charvet, I., Suppasri, A., Kimura, H., Sugawara, D., Imamura, F., 2015. A multivariate generalized linear tsunami fragility model for Kesenuuma City based on maximum flow depths, velocities and debris impact, with evaluation of predictive accuracy. *Nat. Hazards*. <http://dx.doi.org/10.1007/s11069-015-1947-8>.
 Chen, C.L., 1988. Generalized viscoplastic modelling of debris flow. *J. Hydraul. Res.* 114 (3), 237–258.

- Cui, X., Gray, J.M.N.T., 2013. Gravity driven granular free-surface flow around a circular cylinder. *J. Fluid Mech.* 720, 314–337.
- Cui, P., Zeng, C., Lei, Yu, 2015. Experimental analysis on the impact force of viscous debris flow. *Earth Surf. Process. Landf.* 40, 1644–1655. <http://dx.doi.org/10.1002/esp.3744>.
- Faug, T., 2015. Depth-averaged analytic solutions for free-surface granular flows impacting rigid walls down inclines. *Phys. Rev. E* 92. <http://dx.doi.org/10.1103/PhysRevE.92.062310>.
- Faug, T., Naaim, M., Bertrand, D., Lachamp, P., Naaim-Bouvet, F., 2003. Varying dam heights to shorten the run-out of dense avalanche flows: Developing a scaling law from laboratory experiments. *Surv. Geophys.* 24, 555–568.
- Faug, T., Gauer, P., Lied, K., Naaim, M., 2008. About observations of the overrun length of avalanches overtopping catching dams: Cross-comparison of small scale laboratory experiments and observations from full-scale avalanches. *J. Geophys. Res. Atmos.* 113 (F3). <http://dx.doi.org/10.1029/2007JF000854>.
- Faug, T., Chanut, B., Beguin, R., Naaim, M., Thibert, E., Baraudi, D., 2010. A simple analytical model for pressure on obstacles induced by snow avalanches. *Ann. Glaciol.* 51 (54), 1–8.
- Fernandez-Nieto, E.D., Bouchut, F., Bresch, D., Castro Daz, M.J., Mangeney, A., 2008. A new Savage-Hutter type model for submarine avalanches and generated tsunamis. *J. Comput. Phys.* 227 (16), 7720–7754.
- Fischer, J.-T., Kowalski, J., Pudasaini, S.P., 2012. Topographic curvature effects in applied avalanche modeling. *Cold Reg. Sci. Technol.* 74–75, 21–30.
- Gauer, P., Lied, K., Kristensen, K., 2008. On avalanche measurements at the Norwegian full-scale test-site Rytteggfonna. *Cold Reg. Sci. Technol.* 51 (2–3), 138–155.
- Gleirscher, E., Fischer, J.-T., 2014. Retarding avalanches in motion with net structures. *Cold Reg. Sci. Technol.* <http://dx.doi.org/10.1016/j.coldregions.2013.08.007>.
- Gray, J.M.N.T., Wieland, M., Hutter, K., 1999. Gravity-driven free surface flow of granular avalanches over complex basal topography. *Proc. R. Soc. A* 455, 1841–1874.
- Gray, J.M.N.T., Tai, Y.-C., Noella, S., 2003. Shock waves, dead zones and particle-free regions in rapid granular free-surface flows. *J. Fluid Mech.* 491, 161–181. <http://dx.doi.org/10.1017/S00222112003005317>.
- Greve, R., Hutter, K., 1993. Motion of a granular avalanche in a convex and concave curved chute: experiments and theoretical predictions. *Phil. Trans. R. Soc. A* 342. <http://dx.doi.org/10.1098/rsta.1993.0033>.
- Hákonardóttir, K.M., 2004. *The Interaction Between Snow Avalanches and Dams*. University of Bristol, School of Mathematics, Bristol, England (PhD Thesis).
- Hákonardóttir, K.M., Hogg, A.J., 2005. Oblique shocks in rapid granular flows. *Phys. Fluids* 17, 077101. <http://dx.doi.org/10.1063/1.1950688>.
- Hákonardóttir, K.M., Hogg, A.J., Batey, J., Woods, A.W., 2003a. Flying avalanches. *Geophys. Res. Lett.* 30 (23), 2191. <http://dx.doi.org/10.1029/2003GL018172>.
- Hákonardóttir, K.M., Hogg, A.J., Johannesson, T., Tomasson, G.G., 2003b. A laboratory study of the retarding effects of braking mounds on snow avalanches. *J. Glaciol.* 49 (165), 191–200.
- Hákonardóttir, K.M., Hogg, A.J., Johannesson, T., Kren, M., Tiefenbacher, F., 2003c. Large-scale avalanche braking mound and catching dam experiments with snow: a study of the airborne jet. *Surv. Geophys.* 24, 543–554.
- Hungr, O., 1995. A model for the run out analysis of rapid flow slides, debris flows, and avalanches. *Can. Geotech. J.* 32, 610–623.
- Hungr, O., Morgan, G.C., Lellerhals, R., 1984. Qualitative analysis of debris torrent hazards for design of remedial measures. *Can. Geotech. J.* 21 (4), 663–677.
- Hungr, O., Morgan, G.C., Vandine, D.F., Lister, D.R., 1987. Debris flow defenses in British Columbia. In: *Debris Flows/Avalanches: Process, Recognition, and Mitigation*. Reviews in Engineering Geology. 7. pp. 201–222.
- Hutter, K., Svendsen, B., Rickenmann, D., 1996. Debris flow modelling review. *Continuum Mech. Thermo. Dyn.* 8, 1–35.
- Iverson, R.M., 1997. The physics of debris flows. *Rev. Geophys.* 35 (3), 245–296.
- Iverson, R.M., Denlinger, R.P., 2001. Flow of variably fluidized granular masses across three-dimensional terrain: 1. Coulomb mixture theory. *J. Geophys. Res.* 106 (B1), 537–552.
- Jiang, G.S., Tadmor, E., 1998. Non-oscillatory central schemes for multi-dimensional hyperbolic conservation laws. *SIAM. J. Sci. Comput.* 19, 1892–1917.
- Johannesson, T., Gauer, P., Issler, D., Lied, K., 2009. In: Barbolini, M., Domaas, U., Harbitz, C.B., Johannesson, T., Gauer, P., Issler, D., Lied, K., Faug, T., Naaim, M. (Eds.), *The Design of Avalanche Protection Dams*. Recent Practical and Theoretical Developments. European Commission. Directorate General for Research.
- Kafle, J., Pokhrel, P.R., Khattri, K.B., Kattel, P., Tuladhar, B.M., Pudasaini, S.P., 2016. Submarine landslide and particle transport in mountain lakes, reservoirs and hydraulic plants. *Ann. Glaciol.* 57 (71), 232–244. <http://dx.doi.org/10.3189/2016AoG71A034>.
- Kattel, P., Khattri, K.B., Pokhrel, P.R., Kafle, J., Tuladhar, B.M., Pudasaini, S.P., 2016. Simulating glacial lake outburst floods with a two-phase mass flow model. *Ann. Glaciol.* 57 (71), 349–358. <http://dx.doi.org/10.3189/2016AoG71A039>.
- Lie, K.A., Noelle, S., 2003. An improved quadrature rule for the flux-computation in staggered central difference schemes in multidimensions. *J. Sci. Comput.* 18, 69–81.
- Lyu, L., Wang, Z., Cui, P., Xu, M., 2017. The role of bank erosion on the initiation and motion of gully debris flows. *Geomorphology* 285, 137–151. <http://dx.doi.org/10.1016/j.geomorph.2017.02.008>.
- Mergili, M., Fischer, J.-T., Krenn, J., Pudasaini, S.P., 2017. r.avaflow v1, an advanced open-source computational framework for the propagation and interaction of two-phase mass flow. *Geosci. Model Dev.* 10, 553–569. <http://dx.doi.org/10.5194/gmd-10-553-2017>.
- Mergili, M., Emmer, A., Juricova, A., Cochachin, A., Fischer, J.-T., Huggel, C., Pudasaini, S.P., 2018. How well can we simulate complex hydro-geomorphic process chains? The 2012 multi-lake outburst flood in the Santa Cruz Valley (Cordillera Blanca, Peru). *Earth Surf. Process. Landf.* 43, 1373–1389. <http://dx.doi.org/10.1002/esp.4318>.
- Naaim, M., Faug, T., Naaim, F., Eckert, N., 2010. Return period calculation and passive structure design at the Taconnaz avalanche path, France. *Ann. Glaciol.* 51 (54), 89–97.
- Nessyahu, H., Tadmor, E., 1990. Non-oscillatory central differencing for hyperbolic conservation laws. *J. Comput. Phys.* 87 (2), 408–463.
- O'Brien, J.S., Julien, P.Y., Fullerton, W.T., 1993. Two-dimensional water flood and mud flow simulation. *J. Hydraul. Eng.* 119 (2), 244–261.
- Pitman, E.B., Le, L., 2005. A two fluid model for avalanche and debris flows. *Phil. Trans. R. Soc. A* 363 (3), 1573–1601.
- Piton, G., Recking, A., 2016. Design of sediment traps with open check dams. I: Hydraulic and deposition Processes. *J. Hydraul. Eng.* [http://dx.doi.org/10.1061/\(ASCE\)HY.1943-7900.0001048](http://dx.doi.org/10.1061/(ASCE)HY.1943-7900.0001048).
- Pudasaini, S.P., 2012. A general two-phase debris flow model. *J. Geophys. Res.* 117, F03010. <http://dx.doi.org/10.1029/2011JF002186>.
- Pudasaini, S.P., 2014. Dynamics of submarine debris flow and tsunamis. *Acta Mech.* 225, 2423–2434. <http://dx.doi.org/10.1007/s00707-014-1126-0>.
- Pudasaini, S.P., Fischer, J.-T., 2016a. A mechanical erosion model for two-phase mass flows. [arXiv:1610.01806](https://arxiv.org/abs/1610.01806).
- Pudasaini, S.P., Fischer, J.-T., 2016b. A mechanical model for phase-separation in debris flow. [arXiv:1610.03649](https://arxiv.org/abs/1610.03649).
- Pudasaini, S.P., Hutter, K., 2007. *Avalanche Dynamics: Dynamics of Rapid Flows of Dense Granular Avalanches*. Springer, Berlin, New York.
- Pudasaini, S.P., Krautblatter, M., 2014. A two-phase mechanical model for rock-ice avalanches. *J. Geophys. Res. Earth Surf.* 119 (10), 2272–2290. <http://dx.doi.org/10.1002/2014JF003183>.
- Pudasaini, S.P., Wang, Y., Hutter, K., 2005a. Modelling debris flows down general channels. *Nat. Hazards Earth Syst. Sci.* 5, 799–819.
- Pudasaini, S.P., Hsiau, S.-S., Wang, Y., Hutter, K., 2005b. Velocity measurements in dry granular avalanches using particle image velocimetry technique and comparison with theoretical predictions. *Phys. Fluids* 17, 093301. <http://dx.doi.org/10.1063/1.200748>.
- Pudasaini, S.P., Hutter, K., Hsiau, S.-S., Tai, S.-C., Wang, Y., Katzenbach, R., 2007. Rapid flow of dry granular materials down inclined chutes impacting on rigid walls. *Phys. Fluids* 19, 053302. <http://dx.doi.org/10.1063/1.2726885>.
- Savage, S.B., Hutter, K., 1989. The motion of a finite mass of granular material down a rough incline. *J. Fluid Mech.* 199, 177–215.
- Savage, S.B., Hutter, K., 1991. Dynamics of avalanches of granular materials from initiation to runout. Part I. Analysis. *Acta Mech.* 86, 201–223.
- Sovilla, B., Faug, T., Köhler, A., Baroudi, D., Fischer, J.-T., Thibert, E., 2016. Gravitational wet avalanche pressure on pylon like structure. *Cold Reg. Sci. Technol.* <http://dx.doi.org/10.1016/j.coldregions.2016.03.002>.
- Tai, Y.-C., Gray, J.M.N.T., Hutter, K., Noelle, S., 2001. Flow of dense avalanches past obstructions. *Ann. Glaciol.* 32, 281–284.
- Tai, Y.-C., Noella, S., Gray, J.M.N.T., Hutter, K., 2002. Shock-capturing and front tracking methods for granular avalanches. *J. Comput. Phys.* 175 (1), 269–301.
- Takahashi, T., 2007. *Debris Flow: Mechanics, Prediction and Countermeasures*. Taylor and Francis, New York.
- Takahashi, T., 1991. *Debris Flow*. IAHR-AIRH Monograph Series A. Balkema, Rotterdam, Netherlands.
- Teufelsbauer, H., Wang, Y., Chiou, M.C., Wu, W., 2009. Flow-obstacle-interaction in rapid granular avalanches: DEM simulation and comparison with experiment. *Granular Matter* 11 (4), 209–220. <http://dx.doi.org/10.1007/s10035-009-0142-6>.
- Teufelsbauer, H., Wang, Y., Pudasaini, S.P., Borja, R.I., Wu, W., 2011. DEM simulation of impact force exerted by granular flow on rigid structures. *Acta Geotech.* <http://dx.doi.org/10.1007/s11440-011-0140-9>.
- Vagnon, F., Segalini, A., 2016. Debris flow impact estimation on a rigid barrier. *Nat. Hazards Earth Syst. Sci.* 16, 1691–1697. <http://dx.doi.org/10.5194/nhess-16-1691-2016>.
- Viroulet, S., Baker, J.L., Edwards, A.N., Johnson, C.G., Gjaltema, C., Clavel, P., Gray, J.M.N.T., 2017. Multiple solutions for granular flow over a smooth two-dimensional bump. *J. Fluid Mech.* 815, 77–116. <http://dx.doi.org/10.1017/jfm.2017.41>.
- Wawra, M., 2010. *Numerical Modelling of Snow Avalanches: Interaction Between Granular Flow and Obstruction*. University of Soil Culture, Vienna (PhD Thesis).
- Xie, T., Yang, H., Wei, F., Gardner, J.S., Dai, Z., Xie, X., 2014. A new water-sediment separation structure for debris flow defense and its model test. *Bull. Eng. Geol. Environ.* 73, 947–958. <http://dx.doi.org/10.1007/s10064-014-0585-9>.
- Zeng, C., Cui, P., Su, Z.M., Lei, Y., Chen, R., 2014. Failure modes of reinforced concrete columns of buildings under debris flow impact. *Landslides* 1–11. <http://dx.doi.org/10.1007/s10346-014-0490-0>.
- Zhang, S., 1993. A comprehensive approach to observation and prevention of debris flows in China. *Nat. Hazards* 7, 1–23. <http://dx.doi.org/10.1007/BF00595676>.